Supporting Information for

Carbonate-hosted microbial communities are prolific and pervasive methane oxidizers at geologically diverse marine methane seep sites

Jeffrey J. Marlow[1^*], Daniel Hoer[1], Sean Jungbluth[2], Linda Reynard[3‡], Amy Gartman[4], Marko S. Chavez[5], Mohamed Y. El-Naggar[5,6,7], Noreen Tuross[3], Victoria J. Orphan[8], and Peter Girguis[1*]

[1] Department of Organismic and Evolutionary Biology, Harvard University, Cambridge, MA, USA.
[2] Department of Energy, Joint Genome Institute, Walnut Creek, CA, USA.
[3] Department of Human Evolutionary Biology, Harvard University, Cambridge, MA, USA.
[4] U.S. Geological Survey, Santa Cruz, CA, USA.
[5] Department of Physics and Astronomy, University of Southern California, Los Angeles, CA, USA.
[6] Department of Chemistry, University of Southern California, Los Angeles, CA, USA.
[7] Department of Biological Sciences, University of Southern California, Los Angeles, CA, USA.
[8] Division of Geological and Planetary Sciences, California Institute of Technology, Pasadena, CA, USA.
^: Current Address: Department of Biology, Boston University, Boston, MA, USA.
‡: Current Address: Department of Geosciences, Boise State University, Boise, ID, USA.
*: To whom correspondence should be addressed: jjmarlow@bu.edu, pgirguis@oeb.harvard.edu

Keywords: Methane oxidation, Metabolic rates, Endolith, Methane seep

Materials and Methods

Study Sites and Sample Recovery

Gulf of Mexico

The Gulf of Mexico occupies an ancient rift basin, formed between ~120-200 million years ago, which has experienced extensive salt deposition, episodes of carbonate reef formation, and burial caused by continental runoff (*1*). The high organic loading and porous underlying source rock make the region a hydrocarbon-rich basin of high economic interest. Mississippi Canyon is a well-established site of shallow subsurface hydrate deposition and methane and hydrocarbon seepage (*2–4*). During Deep-Submergence Vehicle (DSV) *Alvin* dives 4680 and 4682 of *Atlantis* leg AT 26-12-SVC in March 2014, three carbonate rocks and one push core were collected. Rocks GoM R1 (25x22x12 cm) and GoM R2 (14x10x8 cm) were gray conglomerates cemented by fine-grained matrix; these samples had few visible conduits and were recovered from a small (~1.5 m tall) carbonate mound with intermittent patches of microbial mat (Fig. S1). Rocks GoM R3 and GoM R4 were tan-colored, platy, more cohesive samples approximately 16x12x4 cm and 21x10x5 cm in size, respectively, collected from fractured carbonate pavement underlain by methane hydrate. Push cores GoM PC1 and PC2, recovered from the base of the mound, exhibited fine gray sediment with a dark gray / black horizon between ~6-10 cm depth. During sample processing, all rocks were found to emit small quantities of viscous black oil. (See Fig. S1 for site context and sample images; not all *in situ* locations are shown due to video recording challenges during the *Alvin* Science Verification Cruise.)

U.S. Atlantic Margin

The United States Atlantic margin (USAM) was initiated as a rift zone in the Mesozoic that divided the Pangean supercontinent; subsequent diachronous detachment, spreading, and volcanic overprinting led to distinct faulting and petrological characteristics along eastern North America (*5*). As the type case of a passive margin, the dominant geological forces since the Pliocene have been sedimentation and canyon formation (*6*). The absence of both active subsidence and hydrocarbon basin context made the observation of pervasive seepage a surprise (*7*). Using backscatter data, 570 gas plumes between Cape Hatteras and Georges Bank were detected in 2014, most of which were associated with high relief portions of submarine canyons. The seepage was attributed to “stranded” hydrate deposits upslope of a deepening gas hydrate stability zone (*7*).

Veatch Canyon and New England Seep 2 were detected by backscatter data (*7*) and subsequently investigated by the remotely operated vehicle (ROV) *Deep Discoverer*, which confirmed bubble ebullition, *Bathymodiolus* clams, and, at New England Seep 2, exposed methane hydrate (*8*). During *Atlantis* expedition AT 36 in July and August of 2016, water column backscatter data revealed five actively emitting gas seeps at the New England Seep area and 13 at Veatch Canyon, while enhanced porewater sulfide concentrations and the recovery of putative sulfur oxidizing 16S rRNA genes suggested a dynamic sulfur cycle co-localized with seepage activity (*9*). *DSV Alvin* dives 4828 and 4835 visited Veatch Canyon, while dives 4833 and 4834 targeted New England Seep 2.

At Veatch Canyon, sample VC R1 was collected from a bed of bivalves coated with white microbial mat, both of which are strongly suggestive of chemosynthetic activity (Fig. S2A-B).

Sample VC R2 was recovered from the outer edge of a carbonate outcrop at a site that did not exhibit standard manifestations of methane seepage. Shards of bivalve shells and brown, mat-free sediment cover characterized the site (Fig. S2C-D). At New England Seep 2, sample NES R1 was obtained approximately 1m from an extensive white microbial mat; bivalves were scarce and active bubbling was not observed (Fig. S2E). Sample NES R2 was recovered from a broad, sediment-laden trough with intermittent carbonate fragments (Fig. S2F-G), several dozen meters from the nearest surface expression of seepage.

Guaymas Basin

The Guaymas Basin in the central Gulf of California is a young marginal rift basin marked by the co-occurrence of active seafloor spreading and the input of abundant organics from the overlying water column. Magmatic intrusions thermally alter these sediments to generate fluids rich in organic acids, ammonia, carbon dioxide, and methane and higher hydrocarbons (*10–13*). AOM was previously detected in laboratory incubations using sediment horizons a few centimeters beneath pervasive orange and white sulfide oxidizing microbial mats (*14, 15*). Several ANME and SRB lineages were abundant, including thermotolerant ANME-1-Guaymas methanotrophs (*16*) and the HotSeep-1 sulfate reducing bacteria first detected at Guaymas (*17*).

During *Atlantis* expedition AT 37-06, two areas of extensive biological activity (as indicated by seafloor surface expressions of microbial mats, bivalves, and tubeworms) were sampled, classified here as Guaymas Basin North (GBN) and South (GBS); see Fig. S3. GBN R1 was a poorly lithified rock covered with worm tubes, recovered during dive AD 4864 from the base of a rocky outcrop within a region of sparse white microbial mat (Fig. S3A). Dive AD 4867 visited Guaymas-9A, an off-axis seep with shallow (<1 m) occurrences of methane hydrate. GBN R2 was a white carbonate rock covered with a thin veneer of brown sediment; the sample was collected from a rocky outcrop in a mat-free area approximately two meters from bivalve shell hash and tube worms (Fig. S3B). GBN R3 was a crumbly brown rock recovered at a depth of ~6 cm within a push core of a thick round white mat (Fig. S3C-D); hydrate was observed at ~18 cm depth beneath this feature. GBN PC1 was collected from an area where the sediment surface was covered in small worm burrows, approximately 50 cm from a patch of tube worms (Fig. S3E-F).

At GBS, R1 was collected from Cathedral Hill, a 5-m tall carbonate mound topped with mat-covered sulfide chimney spires and flanked by yellow, orange, and white microbial mats. GBS R1 was characterized by cm-scale holes and internal conduits, and was obtained from a plateau atop the Cathedral Hill mound marked by rocky outcrops covered with brown sediment (Fig. S3G).

California Coast

Two sites of putative chemosynthetic activity were investigated along the transpressional California Borderland, a heavily fragmented active margin boundary where the Pacific and North American tectonic plates experience both compression and strike-slip dynamics (*18–20*). The region's hydrocarbon seepage activity, attributed to both local methanogenesis and the thermal breakdown of larger organic molecules during subduction, has been well established at sites such as Coal Oil Point (*21*) and the Santa Monica Basin (*22*).

The Point Dume seep field is located along the shallow-sloping base of Dume submarine canyon, approximately 8 km southwest of Malibu, CA. Following up on the 2013 recovery of vesicomyid clams and a multibeam survey by the *E/V Nautilus*, a ~1.3 km-long field of white,

yellow, and orange microbial mats, punctuated by dozens of rounded, chimney-like constructions ~0.25-1m in height, was observed by the *ROV Hercules* during an *E/V Nautilus* cruise in August 2015 (*23*). Subsequent sampling during NA-073 in June 2016, NA-084 in August 2017, and R/V *Falkor* leg 163 019 in October 2018 recovered sediment cores and chimney rock structures. Samples PD R1 and PD R2 were disparate samples from a seemingly contiguous structure. PD R1 was the top, rounded portion of a ~25-cm-tall chimney and was covered in orange microbial mat; PD R2 was at the base of the structure, covered in sparse white mat and a thin layer of brown sediment (Fig. S4A-B). PD R4 was a 38-cm-tall chimney structure covered in white microbial mat (Fig. S4C). PD R3 was part of a sedimented carbonate pavement at the top of the gentle slope that hosted most of the microbial mats and chimneys (Fig. S4D-E) and PD PC1 and PD PC2 were collected through white mat-covered sediment at the base of small chimney structures at different areas of the Point Dume seep complex. Fig. S5 provides additional contextual images of the extensive microbial mats and chimney fields at Point Dume.

The Palos Verdes shelf is directly south of Los Angeles; early investigations found evidence of subsurface gas repositories, sulfide-rich fluid, and carbonate rock hardground (*24*, *25*) while more recent exploration surveyed shallow (~350 m depth) near-shore (<5 km) carbonate mounds associated with intermittent bubbling (*26*). The rock samples were collected from an area devoid of surface markers representative of active seepage: PV R1 was a sedimented crustal pavement and PV R2 was the top of a well consolidated chimney-like structure ~25 cm in height (Fig. S4F-H).

Sampling and Analysis Details

Dataset 1 provides details on all sampling sites and indicates which samples were used for designated analyses described in this study.

Site Classification and Sample Processing

At all sampling locations, the designation of an "active seep site" required observation of white microbial mats (which frequently consist of sulfide oxidizing bacteria), clam beds, and/or bubble ebullition; this classification scheme is consistent with previous biological and geological surveys of seeps around the world (*27*, *28*). "Inactive seep sites" lacked all of these surficial manifestations of full methane perfusion of the sediment and rock column, but full methane consumption below the seafloor or temporally intermittent fluid flow cannot be ruled out.

Metabolic Rate Measurements at Pressure

To attain the desired pressure within the custom-built titanium 4L pressure chambers, a high-performance liquid chromatography pump (ChromTech, Inc.) delivered water continuously at 30 mL min^{-1}, and when bubbles were no longer observed in the outflow, vessel pressure was increased to the targeted value (7.58 MPa). Pressure readings were provided by an analog bourdon-style pressure gauge on the outlet of the vessel, as well as on the high-pressure pump itself. Once the target pressure was achieved, the pump was stopped, and high-pressure needle valves on the inlet and outlet fluid lines were immediately closed, isolating the vessel and holding it at the desired pressure. The analog pressure gauge was plumbed between the lid of the vessel and the valve sealing the outflow line, which allowed confirmation and monitoring of the vessel pressure throughout the experiment. Experimental duration was calculated to minimize the proportion of available methane consumed and thereby enable relatively consistent exergonic driving force throughout the incubation. Experiments at saturated methane concentrations

proceeded for one day, while those with a range of methane partial pressures ran for 8 hours. At the designated end point, the pressure in the vessel was vented, the lid was removed, and the experimental Mylar™ bags were extracted. In the anoxic chamber, water was collected for D/H analysis via sterile syringe through the bag and processed and measured as described above.

Anaerobic Oxidation of Methane Rate Comparisons

By conducting an extensive review of previously published AOM rates, we sought to contextualize our experimental results and better understand how endolithic AOM from both active and inactive seep sites compared with sediment-hosted processes. Given the aim of evaluating naturally occurring methane oxidizing potential, only unmodified environmental samples were considered in this analysis; enrichment cultures were excluded. Studies using methane-dependent sulfide production as a proxy for AOM were not included, as this parameter can be decoupled from methane oxidation (*29*, *30*).

For each previously published study, the highest reported rate was first converted to nmol methane oxidized / cm^3 d (see Dataset 2). These values were normalized to the methane concentration used in our long-term incubation experiments (1.1 mM, determined using a temperature-adjusted Henry's law constant of 5.7 x 10^{-6} (*31*)) using equation 1 (*32*):

$$\frac{V_2}{V_1} = \frac{C_2\ (K_M + C_1)}{C_1\ (K_M + C_2)} \qquad \text{Eq. 1}$$

In this formulation, *V* represents the measured or calculated rate of AOM (nmol methane / cm^3 d); *C* signifies the methane concentration (mM); K_M stands for the substrate concentration at which the reaction rate is half of its maximum (mM); and subscripts *1* and *2* represent the parameters at the lower and higher methane concentrations, respectively. K_M values for AOM by environmental communities are poorly constrained. Two empirical efforts to determine K_M in an Eckernförde Bay sediment enrichment (*29*) and Hydrate Ridge seep sediment (*32*) did not attain a V_{max}, meaning that only a poorly constrained lower bound can be established; these were 1.1 and 7.9 mM, respectively. High-pressure incubations of mud volcano sediment produced a sparsely populated AOM kinetic curve from which a K_M of 37 mM was calculated (*33*). *In vitro*, MCR from the methanogen *M. marburgensis* oxidized methane with a K_M of ~10 mM (*34*). Perhaps the most analogous data come from high-rate data from Bowles et al. (*35*), where Gulf of Mexico and Guaymas Basin seep sediments exhibited AOM values of 4800 and 3600 nmol / cm^3 d, respectively. The corresponding K_M values were estimated to be 11 mM and 8, respectively.

Given this dearth of suitable values for AOM mesocosms, we calculated K_M from Point Dume seep sediment subjected to high pressure (1100 psi) and a range of methane concentrations (1.1-129 mM). Based on a linear interpolation between the data points bounding V_{max} / 2, the K_M was calculated to be 5.65 mM. There is likely a degree of sample-to-sample variation in kinetic parameters, but our measured value is on the lower end of proposed K_Ms and lower K_M bounds, making for conservative comparisons (i.e., producing higher normalized rate values for initial studies whose initial concentrations were > 1.1 mM; see Dataset 2).

Conductance Measurements

Before probing the samples, and in between probing each individual sample, the probe tips were rinsed with isopropyl alcohol followed with deionized water, and then dried with

compressed air. To achieve a probe tip separation on the order of tens of microns, a 40 μm diameter wire, measured with digital calipers, was placed across the sample and the two probes used were positioned roughly on either side of the wire. The wire was then removed once the probes were properly in position. This probe separation distance was chosen because it was roughly the distance that spatially separated, but potentially electrically connected, ANME-SRB aggregates appeared in fluorescence microscopy analyses.

Microscopy

To minimize image blurring caused by water movement during long-duration scans, the fragment was attached to the bottom of a small dish with autoclaved clay. Laser power, scan rates, and gain settings were set to minimize background signal; images were acquired and stitched together with Zeiss' ZEN software. (Any use of trade, firm, or product names is for descriptive purposes only and does not imply endorsement by the U.S. Government.) Because background minimization settings were optimized for each field of view, some edge effects between fields of view are present.

Two fields of view are shown in Fig. S8 with identical instrumental and image analysis parameters as in Fig. 3. The substantially brighter emission across the Cy3 and FAM6 spectral windows seen in the experimental samples (Fig. 3) increases our confidence that the signal is due to phylogenetically resolved microorganisms rather than background fluorescence.

Microbial Community Analysis

DNA Extraction, SSU rRNA Gene Amplification, and Illumina Sequencing

To prepare samples for DNA extraction, rocks were powdered (to the approximate particle size of sediment samples) with a sterile ceramic mortar and pestle. Mortar and pestle were washed with bleach, ethanol, and DI H_2O prior to autoclaving between each use. The extraction protocol was modified by bead beating and incubating the samples (4.5 m/s followed by 5 mins at 70° C) twice upon addition of the lysis buffer. Following PCR validation (including positive and negative controls) with the 27F and 1492R primers (*36*), target regions were amplified using 515yF and 806bR primers modified to include the Illumina flowcell adapter sequences (*37*). Forward primers contained an additional 8-bp barcode to assign individual sequences to specific samples. Each 25 μl PCR reaction was prepared in OneTaq 2x Master Mix (NEB, Ipswich, MA) with 2 μl of 5 μM forward and reverse primers and 1 μl of genomic DNA template. PCR cycling conditions consisted of an initial denaturation step at 94°C for 3 min, followed by 35 cycles of 94°C denaturation for 45 sec, 50°C annealing for 1 min, 72°C extension for 1.5 min, and a final extension step at 72°C for 10 min. With each PCR run, a positive control with *E. coli* genomic DNA and a negative control using 1 μl of water instead of DNA template were run. Amplification products were subsequently purified using the Aurora system (Boreal Genomics, Vancouver, BC) with the clean-up protocol delineated in the manufacturer's instructions, and quantified using the Qubit 2.0 fluorometer (Invitrogen, Carlsbad, CA). Purified amplicons were diluted to equal concentrations and were sequenced (2 x 250 bp) on an Illumina (San Diego, CA, USA) MiSeq sequencer at RTL Genomics (Lubbock, TX, USA).

Read Processing, Clustering with UCLUST and Deblur, and Taxonomic Assignment

Forward and reverse reads were merged together using PEAR (*38*) with default parameters. Quality-trimming of the reads was performed using a custom tool developed at RTL Genomics

to trim reads with a sliding window approach to trim at the last base where the total average is greater than 25. Sample-specific barcoded regions, represented by the first eight base pairs of sequence, were manually removed. Removal of chimeric sequences was performed using USEARCH v7.0.1090 (*39*) to screen quality-filtered paired reads based on matches to a version of the SILVA v128 SSURef database (*40*) expunged of all sequences with pintail quality <50 and alignment quality <75.

Sequence clustering at 97% identity was performed with UCLUST (v1.2.22q; (*39*)) in QIIME (v1.9.1; (*41*)) on all non-chimeric paired-end reads. The most abundant sequences in each cluster were selected as the representative sequences, which were then assigned taxonomy in QIIME using assign_taxonomy.py and the chimera-screened SILVA v128 SSURef database described above with parameters "similarity: 0.9", "uclust_max_accepts: 10", and "min_consensus_fraction: 0.90".

Single Nucleotide Resolution Approaches

Three methods – UCLUST, Deblur, and DADA2 – were assessed for their ability to produce error-free sequence clusters. Sequence clustering with Deblur (v1.0.3; (*42*)) was performed in "workflow" mode with parameter "t=247"; Deblur employs VSEARCH (v2.6.0; (*43*)), SortMeRNA (v2.0; (*44*)), and MAFFT (v7.310; (*45*)) to perform clustering. All Deblur clusters were assigned taxonomy as described above.

Unpaired forward and reverse reads with primers removed were used as input into DADA2 (v1.6.0; (*46*)) and processed according to an online tutorial (https://benjjneb.github.io/dada2/tutorial.html). The "filterAndTrim" script was run with parameters: "truncLen=c(240,160)", "maxN=0", maxEE=c(2,2)", "truncQ=2", "rm.phix=TRUE". Chimeric sequences were removed using the "removeBimeraDenovo" script using the "consensus" method. Taxonomic assignment of sequences was performed using the "assignTaxonomy" script and the "silva_nr_v128_train_set.fa" database provided with DADA2.

To evaluate the fidelity of error-free sequence cluster generation, all sequences representing clusters from the different clustering methods were compared using BLAST (parameters: e-value 1e-5, max_target_seqs 1) to the chimera-checked SILVA v128 database described above. Deblur was chosen as the clustering method because it resulted in the fewest number of mismatches to the target database (Fig. S9).

Alpha and Beta Diversity

To prepare for using the "Phylogenetic Diversity PD" metric, all Deblur clusters were aligned using MUSCLE (v3.8.31; (*47*)) and a phylogeny was generated using FastTree (v2.1.3; (*48*)) with default parameters. Alpha diversity metrics (i.e., Observed Species, Whole Tree PD, and Chao1) were all calculated in QIIME using the alpha_diversity.py script and samples rarefied to an even sampling depth (n=2658 sequences).

Non-metric multi-dimensional scaling analysis (NMDS) was performed in QIIME using the scripts beta_diversity_through_plots.py and nmds.py with multiple diversity metrics: Bray-Curtis, binary Jaccard, and unweighted UniFrac. Unweighted diversity metrics were applied because DADA2 had not been benchmarked for use in weighted analyses at the time of analysis. Sequences were not rarefied to an even sampling depth prior to analysis.

Community Statistical Analysis

Statistical analyses were performed using paired reads rarefied to an even depth across all samples (n=2658 reads). Comparisons by location, lithology, mineralogy, and methane oxidation rates were explored using PERMANOVA tests (1000 permutations) with the QIIME script compare_categories.py (Table S6). Dissimilarity between microbial diversity and community structure and associated methane oxidation rates was explored using Mantel tests with 1000 replications performed in QIIME using the scripts distrance_matrix_from_mapping.py and compare_distance_matrices.py (Table S7).

Phylogenetic Analysis

All Deblur clusters that were found in ≥5% abundance in any single sample (n=32) were manually queried through NCBI BLAST (*49*) on November 18, 2017 (default parameters), to identify closest database matches. The single best match for each sequence was identified using the following criteria, which were employed sequentially in the event of a tie: 1) top bitscore match, 2) top similarity percent, 3) preference for sequences derived from isolates, 4) first clone published with an accompanying (i.e., citable) manuscript, 5) preference for clones generated by the corresponding study's lead author, and 6) no requirement for a citable manuscript. The search revealed 32 unique sequences, which were aligned with the 32 Deblur cluster sequences using the online SINA aligner (v1.2.11; (*50*)). Alignment positions corresponding to ends extending beyond the range of the amplicon were removed and a phylogeny was constructed in ARB (v6.0.4; (*51*)) using RAxML (v7.7.2; (*52*)) with the GTR model of nucleotide substitution under the gamma- and invariable- models of rate heterogeneity, and selecting the best tree from 100 replicate runs. The phylogeny and associated abundance data were visualized using R (v3.4.1; (*53*)) and the pheatmap package (v1.0.8).

Data Archiving

Sample metadata and the SSU rRNA sequence files used in this study were submitted to the NCBI BioSample and Sequence Read Archive databases and are accessible via BioProject identifier PRJNA648152.

Supplementary Text

Calculating Methane Concentrations in Incubation Experiments

Dissolved methane concentration is a key factor to consider when designing rate-based experiments and establishing the environmental relevance of resulting data. Gas concentration in the aqueous phase (c_a, in mol / m^3) is calculated as the product of the partial pressure of the gas species under equilibrium conditions (p, in Pa) and the Henry's law constant H^{cp} (mol / m^3 Pa):

$$c_a = p * H^{cp} \quad \text{Eq. 2}$$

Henry's law constants depend on the gas and solvent species as well as temperature and salinity. H^{cp} for methane under standard conditions (p = 101325 Pa, T = 298.15 K) in pure water was taken from an exhaustive compilation of empirical and theoretical data (*31*). We used the median value of 29 data points: 1.4×10^{-5} mol / m^3 Pa.

The temperature correction (Eq. 3) is derived from the Van't Hoff equation, which relates equilibrium values to changes in temperature (T).

$$H_T^{cp} = H_{298.15}^{cp} * exp\left(\frac{d(\ln H^{cp})}{d\left(\frac{1}{T}\right)} * \left(\frac{1}{T} - \frac{1}{298.15}\right)\right) \quad \text{Eq. 3}$$

The median value for d(lnH^{cp}) / d(1/T), based on 18 different studies as reported in Sander, 2015 (*31*), was 1600 K. The Henry's law constant at 4 °C (277.15 K), the temperature at which AOM rate experiments were conducted, was calculated to be 2.1x10^{-5} mol / m^3 Pa.

Most gases exhibit decreased solubility as the salinity of the solvent is increased. The relationship can be described with a modified Sechenov equation that accounts for mixed ion solutions such as seawater (Eq. 4, (*54*)).

$$\log\left(\frac{c_{G,0}}{c_G}\right) = \sum c_i \, (h_i + h_G) \quad \text{Eq. 4}$$

In this formulation, $c_{G,0}$ and c_G signify the gas concentration in pure water and the salt solution, respectively. For each ion in solution, c_i represents the molar concentration and h_G and h_i denote gas and ion-specific constants, respectively. The values of these ion-specific parameters are provided in Table S9 using the composition of Standard Seawater (*55*), a temperature- and salinity- corrected seawater density equation from Millero & Poisson (*56*), and h_G and h_i values from Weisenberger & Schumpe (*57*). The resulting calculation for methane gas provides the dissolved concentration correction factor needed to account for the ionic composition of seawater:

$$c_G = \frac{c_{G,0}}{1.2329} \quad \text{Eq. 5}$$

Taking temperature and medium composition into account, H^{cp} for methane in our incubations was 1.7x10^{-5} mol / m^3 Pa. This value was used according to equation 2 to determine the dissolved concentration of methane in all experiments.

Developing a Framework for Assessing Methanotrophic Rates

In order to identify factors that could account for different metabolic rates among samples, a conceptual framework was developed. We anticipate that this framework will identify relevant variables for future investigation when thorough analysis is beyond the scope of this study.

AOM metabolic modeling efforts have sought to explain methane oxidizing rates (R_{AOM}) based on environmental parameters; the most robust combine kinetic and thermodynamic terms, as in equation 6 (*58*).

$$R_{AOM} = V_{max} \, F_K \, F_T \quad \text{Eq. 6}$$

In this formulation, V_{max} represents the maximum rate of the reaction, when all available (rate-limiting) enzymes are saturated with substrate. This maximal rate is tempered by both kinetic (F_K) and thermodynamic (F_T) factors, which are shown in equations 7 and 8, respectively.

$$F_K = \left(\frac{[CH_4]}{K_M^{methane} + [CH_4]}\right)\left(\frac{[SO_4^{2-}]}{K_M^{sulfate} + [SO_4^{2-}]}\right) \quad \text{Eq. 7}$$

$$F_T = \frac{1}{\exp\left(\frac{\Delta G_r + F\Delta\Psi}{RT}\right)+1} \quad \text{Eq. 8}$$

In the kinetic term, [CH_4] and [SO_4^{2-}] indicate the concentrations of methane and sulfate, respectively, and K_M values signify Michaelis-Menten constants, or the substrate concentration at which the reaction rate is V_{max} / 2. In the thermodynamic term, which accounts for slower reaction rates near equilibrium using Fermi-Dirac statistics (*59*), ΔG_r represents the Gibbs energy of the AOM reaction, $\Delta\Psi$ indicates the potential across the cell membrane, F stands for the Faraday constant, R the gas constant, and T the temperature (K).

The Gibbs energy quantifies the overall amount of energy required by or liberated from a given reaction. Large absolute values reveal that reactants and products are far from equilibrium while the sign indicates whether the reaction is endergonic ($+\Delta G_r$) or exergonic ($-\Delta G_r$). Gibbs energies are calculated as shown in equation 9,

$$\Delta G_r = RT \ln\left(\frac{Q}{K}\right) \quad \text{Eq. 9}$$

in which K denotes the equilibrium constant and Q, determined by equation 10, represents the reaction quotient.

$$Q = \prod_i a_i^{Vi} \quad \text{Eq. 10}$$

Here, a_i indicates the activity of the ith species and Vi signifies the stoichiometric coefficient of the ith species. For AOM, Q is calculated as

$$Q = \frac{a_{bicarbonate}\ a_{sulfide}\ a_{water}}{a_{methane}\ a_{sulfate}} \quad \text{Eq. 11}$$

where activity values are determined by the product of molalities (m) and activity coefficients (γ):

$$a_i = m_i\ \gamma_i \quad \text{Eq. 12}$$

Equations 6-12 can be used as the theoretical basis of comparison between samples, exposing several parameters as potential differentiators. The variables whose increase would enhance R_{AOM} are V_{max}, [CH_4], [SO_4^{2-}], T, $a_{methane}$, and $a_{sulfate}$; those inversely related to R_{AOM} are methane and sulfate's K_M values, $\Delta\Psi$, $a_{bicarbonate}$, $a_{sulfide}$, and a_{water}. Activity values are a function of molal concentration and activity coefficients, which in turn depend on the solution's temperature and ionic strength as determined by an extended version of the Debye-Huckel equation (*60*). Across all initial rate incubation experiments, temperature and pressure were consistent and thus not relevant as differentiating variables. Advective transport is an additional, frequently dominant, aspect of rate-determining reaction transport models (*58*, *61*), but is not included in this analysis because of the batch nature of the incubations.

The bulk values of abiotic factors [CH_4], [SO_4^{2-}], $a_{methane}$, $a_{sulfate}$, $a_{bicarbonate}$, $a_{sulfide}$, and a_{water} were ostensibly consistent between treatments, but the physicochemical context of an organism's immediate surroundings on the microscale could vary based on the composition of the substrate. For example, organic carbon content exhibits a positive correlation with methane adsorption to shale rock surfaces – potentially due to hydrophobic interactions (*62*, *63*) – an effect that is enhanced with increased porosity (*64*).

Kinetically relevant biotic parameters include V_{max} and K_M, as well as additional factors not explicitly included in equations 6-12. V_{max} and K_M values for carbonate rock sample PD R3 and sediment sample PD PC2 were investigated by measuring methane oxidation rates across a range of methane concentrations (Fig. S6). K_M is formally defined as the ratio of the rate of dissociation of an enzyme-substrate complex (through forward or backward reactions) to its rate of formation, and is thus most directly relevant to enzyme kinetics on a single cell or single molecule scale (*65*). Estimating and interpreting K_M values from the kinetic data is a challenge in the context of complex microbial communities, as multiple K_Ms can co-exist. Indeed, the PD R3 data in Fig. S6 could point to a multi-modal system in which kinetics at low methane concentrations (<~45 mM) are consistent with sediment-based communities, but at higher concentrations, heightened methane oxidation rates are possible.

Given the likely role of direct electron transfer in enabling sulfate-coupled AOM (*66*, *67*), cell adherence to conductive solid substrates could facilitate the rapid exchange of reducing equivalents, thereby increasing V_{max}. While the rate of this potential electron delivery mechanism through carbonate rocks – several of which contain appreciable quantities of iron-bearing pyrite (Table S2) – remains uncertain, the ability to maintain syntrophic partners across multiple cell lengths could overcome temporal and spatial interruptions in reactant supply. An apparent segregation of ANME and SRB was recently reported on electrically conductive carbon cloth (*68*), and some monospecific aggregations were observed along rock pore spaces of the pyrite-rich PD R1 (Figs. 3, S7), suggesting that direct contact with the rock's surface may sustain methane-oxidizing and sulfate-reducing metabolism.

The influence of particular interspecies interactions on AOM rates – either indirectly through reactant supply or product drawdown or directly through as-yet-uncharacterized hydrocarbon metabolic pathways – remains an intriguing prospect. In this context, our data signify a useful starting point for testing the roles of specific lineages.

References

1. A. Salvador, Origin and development of the Gulf of Mexico basin. *The gulf of Mexico basin*, 389–444 (1991).

2. W. T. Wood, P. E. Hart, D. R. Hutchinson, N. Dutta, F. Snyder, R. B. Coffin, J. F. Gettrust, Gas and gas hydrate distribution around seafloor seeps in Mississippi Canyon, Northern Gulf of Mexico, using multi-resolution seismic imagery. *Marine and Petroleum Geology*. **25**, 952–959 (2008).

3. K. G. Lloyd, D. B. Albert, J. F. Biddle, J. P. Chanton, O. Pizarro, A. Teske, Spatial structure and activity of sedimentary microbial communities underlying a Beggiatoa spp. mat in a Gulf of Mexico hydrocarbon seep. *PLoS One*. **5**, e8738 (2010).

4. R. Coffin, L. Hamdan, R. Plummer, J. Smith, J. Gardner, R. Hagen, W. Wood, Analysis of methane and sulfate flux in methane-charged sediments from the Mississippi Canyon, Gulf of Mexico. *Marine and Petroleum Geology*. **25**, 977–987 (2008).

5. M. O. Withjack, R. W. Schlische, (SEPM, 2005), pp. 203–235.

6. J. Obelcz, D. Brothers, J. Chaytor, U. ten Brink, S. W. Ross, S. Brooke, Geomorphic characterization of four shelf-sourced submarine canyons along the US Mid-Atlantic continental margin. *Deep Sea Research Part II: Topical Studies in Oceanography*. **104**, 106–119 (2014).

7. A. Skarke, C. Ruppel, M. Kodis, D. Brothers, E. Lobecker, Widespread methane leakage from the sea floor on the northern US Atlantic margin. *Nature Geoscience*. **7**, 657–661 (2014).

8. A. M. Quattrini, M. S. Nizinski, J. D. Chaytor, A. W. Demopoulos, E. B. Roark, S. C. France, J. A. Moore, T. Heyl, P. J. Auster, B. Kinlan, Exploration of the canyon-incised continental margin of the northeastern United States reveals dynamic habitats and diverse communities. *PloS one*. **10**, e0139904 (2015).

9. D. McVeigh, A. Skarke, A. Dekas, C. Borrelli, W.-L. Hong, J. Marlow, A. Pasulka, S. Jungbluth, R. Barco, A. Djurhuus, Characterization of benthic biogeochemistry and ecology at three methane seep sites on the northern US Atlantic margin. *Deep Sea Research Part II: Topical Studies in Oceanography* (2018).

10. J. K. Whelan, B. R. Simoneit, M. E. Tarafa, C1C8 hydrocarbons in sediments from Guaymas Basin, Gulf of California—Comparison to Peru Margin, Japan Trench and California Borderlands. *Organic geochemistry*. **12**, 171–194 (1988).

11. K. von Von Damm, J. t Edmond, C. Measures, B. Grant, Chemistry of submarine hydrothermal solutions at Guaymas Basin, Gulf of California. *Geochimica et Cosmochimica Acta*. **49**, 2221–2237 (1985).

12. C. S. Martens, Generation of short chain acid anions in hydrothermally altered sediments of the Guaymas Basin, Gulf of California. *Applied Geochemistry*. **5**, 71–76 (1990).

13. F. Dowell, Z. Cardman, S. Dasarathy, M. Y. Kellermann, J. S. Lipp, S. E. Ruff, J. F. Biddle, L. J. McKay, B. J. MacGregor, K. G. Lloyd, Microbial communities in methane-and short chain alkane-rich hydrothermal sediments of Guaymas Basin. *Frontiers in microbiology*. **7** (2016).

14. J. Kallmeyer, A. Boetius, Effects of Temperature and Pressure on Sulfate Reduction and Anaerobic Oxidation of Methane in Hydrothermal Sediments of Guaymas Basin. *Applied and Environmental Microbiology*. **70**, 1231–1233 (2004).

15. M. Y. Kellermann, G. Wegener, M. Elvert, M. Y. Yoshinaga, Y.-S. Lin, T. Holler, X. P. Mollar, K. Knittel, K.-U. Hinrichs, Autotrophy as a predominant mode of carbon fixation in

anaerobic methane-oxidizing microbial communities. *Proceedings of the National Academy of Sciences*. **109**, 19321–19326 (2012).

16. J. F. Biddle, Z. Cardman, H. Mendlovitz, D. B. Albert, K. G. Lloyd, A. Boetius, A. Teske, Anaerobic oxidation of methane at different temperature regimes in Guaymas Basin hydrothermal sediments. *ISME J*. **6**, 1018–1031 (2012).

17. T. Holler, F. Widdel, K. Knittel, R. Amann, M. Y. Kellermann, K.-U. Hinrichs, A. Teske, A. Boetius, G. Wegener, Thermophilic anaerobic oxidation of methane by marine microbial consortia. *ISME J*. **5**, 1946–1956 (2011).

18. J. Vedder, Regional geology and petroleum potential of the southern California borderland (1987).

19. D. G. Moore, Reflection profiling studies of the California continental borderland: structure and Quaternary turbidite basins. *Geological Society of America Special Papers*. **107**, 1–136 (1969).

20. P. Eichhubl, H. G. Greene, N. Maher, Physiography of an active transpressive margin basin: high-resolution bathymetry of the Santa Barbara basin, Southern California continental borderland. *Marine Geology*. **184**, 95–120 (2002).

21. J. S. Hornafius, D. Quigley, B. P. Luyendyk, The world's most spectacular marine hydrocarbon seeps (Coal Oil Point, Santa Barbara Channel, California): Quantification of emissions. *Journal of Geophysical Research: Oceans*. **104**, 20703–20711 (1999).

22. C. K. Paull, W. R. Normark, W. Ussler III, D. W. Caress, R. Keaten, Association among active seafloor deformation, mound formation, and gas hydrate growth and accumulation within the seafloor of the Santa Monica Basin, offshore California. *Marine Geology*. **250**, 258–275 (2008).

23. K. L. C. Bell, M. L. Brennan, J. Flanders, N. A. Raineault, K. Wagner, *New Frontiers in Ocean Exploration: The E/V Nautilus and NOAA Ship Okeanos Explorer, 2015 Field Season* (Oceanography Society, 2016).

24. D. G. Moore, Acoustic-reflection studies of the continental shelf and slope off southern California. *Geological Society of America Bulletin*. **71**, 1121–1136 (1960).

25. M. A. Hampton, H. A. Karl, C. J. Murray, Acoustic profiles and images of the Palos Verdes margin: implications concerning deposition from the White's Point outfall. *Continental Shelf Research*. **22**, 841–857 (2002).

26. L. Levin, P. R. Girguis, C. R. German, M. L. Brennan, S. Tuzun, J. Wagner, C. Smart, A. Kruger, K. Inderbitzen, J. Le, Exploration and discovery of methane seeps and associated communities in the California Borderland. *Oceanography*, 40–43 (2016).

27. D. H. Case, A. L. Pasulka, J. J. Marlow, B. M. Grupe, L. A. Levin, V. J. Orphan, Methane seep carbonates host distinct, diverse, and dynamic microbial assemblages. *MBio*. **6**, e01348-15 (2015).

28. Treude, Boetius, Knittel, Wallmann, Jorgensen, Anaerobic oxidation of methane above gas hydrates at Hydrate Ridge, NE Pacific Ocean. *Mar Ecol Prog Ser*. **264**, 1–14 (2003).

29. R. J. Meulepas, C. G. Jagersma, Y. Zhang, M. Petrillo, H. Cai, C. J. Buisman, A. J. Stams, P. N. Lens, Trace methane oxidation and the methane dependency of sulfate reduction in anaerobic granular sludge. *FEMS microbiology ecology*. **72**, 261–271 (2010).

30. J. Marlow, A. Kumar, B. Enalls, L. Reynard, N. Tuross, G. Stephanopoulos, P. Girguis, Harnessing a Methane-Fueled, Sediment-Free Mixed Microbial Community for Utilization of Distributed Sources of Natural Gas. *Biotechnology & Bioengineering*. **115**, 1450-1464 (2018).

31. R. Sander, Compilation of Henry's law constants (version 4.0) for water as solvent. *Atmospheric Chemistry & Physics*. **15** (2015).

32. K. Nauhaus, A. Boetius, M. Krüger, F. Widdel, In vitro demonstration of anaerobic oxidation of methane coupled to sulphate reduction in sediment from a marine gas hydrate area. *Environmental Microbiology*. **4**, 296–305 (2002).

33. Y. Zhang, J.-P. Henriet, J. Bursens, N. Boon, Stimulation of in vitro anaerobic oxidation of methane rate in a continuous high-pressure bioreactor. *Bioresource Technology*. **101**, 3132–3138 (2010).

34. S. Scheller, M. Goenrich, R. Boecher, R. K. Thauer, B. Jaun, The key nickel enzyme of methanogenesis catalyses the anaerobic oxidation of methane. *Nature*. **465**, 606–608 (2010).

35. M. Bowles, V. Samarkin, K. Hunter, N. Finke, A. Teske, P. Girguis, S. Joye, Remarkable capacity for anaerobic oxidation of methane at high methane concentration. *Geophysical Research Letters*. **46**, 12192–12201 (2019).

36. W. G. Weisburg, S. M. Barns, D. A. Pelletier, D. J. Lane, 16S ribosomal DNA amplification for phylogenetic study. *Journal of bacteriology*. **173**, 697–703 (1991).

37. S. T. Bates, D. Berg-Lyons, J. G. Caporaso, W. A. Walters, R. Knight, N. Fierer, Examining the global distribution of dominant archaeal populations in soil. *The ISME journal*. **5**, ismej2010171 (2010).

38. J. Zhang, K. Kobert, T. Flouri, A. Stamatakis, PEAR: a fast and accurate Illumina Paired-End reAd mergeR. *Bioinformatics*. **30**, 614–620 (2013).

39. R. C. Edgar, Search and clustering orders of magnitude faster than BLAST. *Bioinformatics*. **26**, 2460–2461 (2010).

40. C. Quast, E. Pruesse, P. Yilmaz, J. Gerken, T. Schweer, P. Yarza, J. Peplies, F. O. Glöckner, The SILVA ribosomal RNA gene database project: improved data processing and web-based tools. *Nucleic acids research*. **41**, D590–D596 (2013).

41. J. G. Caporaso, J. Kuczynski, J. Stombaugh, K. Bittinger, F. D. Bushman, E. K. Costello, N. Fierer, A. G. Pena, J. K. Goodrich, J. I. Gordon, QIIME allows analysis of high-throughput community sequencing data. *Nature methods*. **7**, 335–336 (2010).

42. A. Amir, D. McDonald, J. A. Navas-Molina, E. Kopylova, J. T. Morton, Z. Zech Xu, E. P. Kightley, L. R. Thompson, E. R. Hyde, A. Gonzalez, R. Knight, Deblur Rapidly Resolves Single-Nucleotide Community Sequence Patterns. *mSystems*. **2** (2017), doi:10.1128/mSystems.00191-16.

43. T. Rognes, T. Flouri, B. Nichols, C. Quince, F. Mahé, VSEARCH: a versatile open source tool for metagenomics. *PeerJ*. **4**, e2584 (2016).

44. E. Kopylova, L. Noé, H. Touzet, SortMeRNA: fast and accurate filtering of ribosomal RNAs in metatranscriptomic data. *Bioinformatics*. **28**, 3211–3217 (2012).

45. K. Katoh, K. Misawa, K. Kuma, T. Miyata, MAFFT: a novel method for rapid multiple sequence alignment based on fast Fourier transform. *Nucleic acids research*. **30**, 3059–3066 (2002).

46. B. J. Callahan, P. J. McMurdie, M. J. Rosen, A. W. Han, A. J. A. Johnson, S. P. Holmes, DADA2: high-resolution sample inference from Illumina amplicon data. *Nature methods*. **13**, 581–583 (2016).

47. R. C. Edgar, MUSCLE: multiple sequence alignment with high accuracy and high throughput. *Nucleic acids research*. **32**, 1792–1797 (2004).

48. M. N. Price, P. S. Dehal, A. P. Arkin, FastTree 2–approximately maximum-likelihood trees for large alignments. *PloS one*. **5**, e9490 (2010).

49. C. Camacho, G. Coulouris, V. Avagyan, N. Ma, J. Papadopoulos, K. Bealer, T. L. Madden, BLAST+: architecture and applications. *BMC bioinformatics*. **10**, 421 (2009).

50. E. Pruesse, J. Peplies, F. O. Glöckner, SINA: accurate high-throughput multiple sequence alignment of ribosomal RNA genes. *Bioinformatics*. **28**, 1823–1829 (2012).

51. W. Ludwig, O. Strunk, R. Westram, L. Richter, H. Meier, Yadhukumar, A. Buchner, T. Lai, S. Steppi, G. Jobb, W. Förster, I. Brettske, S. Gerber, A. W. Ginhart, O. Gross, S. Grumann, S. Hermann, R. Jost, A. König, T. Liss, R. Lüßmann, M. May, B. Nonhoff, B. Reichel, R. Strehlow, A. Stamatakis, N. Stuckmann, A. Vilbig, M. Lenke, T. Ludwig, A. Bode, K. Schleifer, ARB: a software environment for sequence data. *Nucleic Acids Research*. **32**, 1363–1371 (2004).

52. A. Stamatakis, RAxML-VI-HPC: maximum likelihood-based phylogenetic analyses with thousands of taxa and mixed models. *Bioinformatics*. **22**, 2688–2690 (2006).

53. R. C. Team, R: A language and environment for statistical computing. Vienna, Austria: R Foundation for Statistical Computing; 2014 (2014).

54. A. Schumpe, The estimation of gas solubilities in salt solutions. *Chemical Engineering Science*. **48**, 153–158 (1993).

55. F. J. Millero, R. Feistel, D. G. Wright, T. J. McDougall, The composition of Standard Seawater and the definition of the Reference-Composition Salinity Scale. *Deep Sea Research Part I: Oceanographic Research Papers*. **55**, 50–72 (2008).

56. F. J. Millero, A. Poisson, International one-atmosphere equation of state of seawater. *Deep Sea Research Part A. Oceanographic Research Papers*. **28**, 625–629 (1981).

57. S. Weisenberger, A. Schumpe, Estimation of gas solubilities in salt solutions at temperatures from 273 K to 363 K. *AIChE J.* **42**, 298–300 (1996).

58. P. Regnier, A. W. Dale, S. Arndt, D. E. LaRowe, J. Mogollón, P. Van Cappellen, Quantitative analysis of anaerobic oxidation of methane (AOM) in marine sediments: A modeling perspective. *Earth-Science Reviews*. **106**, 105–130 (2011).

59. D. E. LaRowe, A. W. Dale, J. P. Amend, P. Van Cappellen, Thermodynamic limitations on microbially catalyzed reaction rates. *Geochimica et Cosmochimica Acta*. **90**, 96–109 (2012).

60. H. C. Helgeson, Thermodynamics of hydrothermal systems at elevated temperatures and pressures. *American Journal of Science*. **267**, 729–804 (1969).

61. J. J. Marlow, D. E. LaRowe, B. L. Ehlmann, J. P. Amend, V. J. Orphan, The potential for biologically catalyzed anaerobic methane oxidation on ancient Mars. *Astrobiology*. **14**, 292–307 (2014).

62. T. Zhang, G. S. Ellis, S. C. Ruppel, K. Milliken, R. Yang, Effect of organic-matter type and thermal maturity on methane adsorption in shale-gas systems. *Organic geochemistry*. **47**, 120–131 (2012).

63. D. J. Ross, R. M. Bustin, The importance of shale composition and pore structure upon gas storage potential of shale gas reservoirs. *Marine and Petroleum Geology*. **26**, 916–927 (2009).

64. J. Xiong, X. Liu, L. Liang, Q. Zeng, Methane adsorption on carbon models of the organic matter of organic-rich shales. *Energy & Fuels*. **31**, 1489–1501 (2017).

65. B. P. English, W. Min, A. M. Van Oijen, K. T. Lee, G. Luo, H. Sun, B. J. Cherayil, S. Kou, X. S. Xie, Ever-fluctuating single enzyme molecules: Michaelis-Menten equation revisited. *Nature chemical biology*. **2**, 87–94 (2006).

66. S. E. McGlynn, G. L. Chadwick, C. P. Kempes, V. J. Orphan, Single cell activity reveals direct electron transfer in methanotrophic consortia. *Nature*. **526**, 531–535 (2015).

67. G. Wegener, V. Krukenberg, D. Riedel, H. E. Tegetmeyer, A. Boetius, Intercellular wiring enables electron transfer between methanotrophic archaea and bacteria. *Nature*. **526**, 587–590 (2015).

68. J. J. Marlow, A. Kumar, B. Enalls, L. M. Reynard, N. Tuross, G. Stephanopoulos, P. Girguis, Harnessing a Methane-Fueled, Sediment-Free Mixed Microbial Community for Utilization of Distributed Sources of Natural Gas. *Biotechnology and bioengineering* (2018).

Supplemental Figure Captions

Fig. S1: Geographic setting and site context of the Gulf of Mexico samples used in this study. Maximum depths of the bathymetric maps are 3902m (upper left) and 2552m (upper right). A) The carbonate mound from which GoM R1 and R2 were collected; mound is approximately 1.5 m tall, and scale bar is 1 m in length. B) Sample GoM R1 immediately after collection. C) The collection site for samples GoM R3 and R4. D) Inset of C marked by orange box; arrow points to outcropping methane hydrate. Scale bars in C and D are 50 cm. E) Sample GoM R3 immediately after collection.

Fig. S2: Geographic setting and site context of the U.S. Atlantic Margin samples used in this study. Bathymetric maps show the shelf-slope break along this passive margin; maximum depths are 2818 m (upper left) and 1932 m (upper right). A) and B) show the VC R1 collection site, which was marked by bivalve shells and white microbial mat characteristic of active seep sites; scale bars are 1 m and 50 cm, respectively. C) and D) reveal the VC R2 collection site, devoid of traditional signs of methane seepage; scale bars are 1 m and 50 cm, respectively. E) shows the NES R1 collection site, on the edge of a white microbial mat (visible in upper left of image; scale bar 1m). F) and G) depict the native position of sample NES R2, recovered from a site approximately 50 m from the nearest sign of seepage; scale bars are 1 m and 10 cm, respectively.

Fig. S3: Geographic setting and site context of the Guaymas Basin samples used in this study. The bathymetric map shows the Guaymas Basin North and South sites situated in the central Gulf of California. The maximum depth of the region bounded by the map is 2050 m. A) Collection site of sample GBN R1, a poorly lithified rock associated with abundant worm tubes. B) The rocky outcrop from which sample GBN R2 was collected had a thin covering of brown sediment. C) and D) show the push core site within a circular white mat from which sample GBN R3 was recovered. E) was taken during collection of GBN PC1 within a patch of worm burrows covered by thin white mat, adjacent to a patch of tube worms. F) GBN PC1 on deck, immediately after recovery. G) shows the collection of rock sample GBS R1, from Cathedral Hill. Image A-E scale bars are 1 m; G scale bar is 10 cm.

Fig. S4: Geographic setting and site context of the California Coast samples used in this study. The bathymetric maps show the Point Dume and Palos Verdes sites situated within the California Borderlands active transpressional margin; maximum depths are 4657 m (upper left map) and 1915 m (upper right). Samples PD R1, PD R2, and PD R4 were microbial mat-covered chimney samples. PD R1 and PD R2 are shown in situ (A) and during collection (B, PD R1 only). C) PD R4 is shown prior to incubation set up, in a lab-based anoxic chamber. D-E) PD R3

was a shallowly buried piece of overhanging carbonate pavement. At Palos Verdes, PV R1 and PV R2 were recovered from an area showing no signs of active seepage. PV R1 was buried carbonate pavement (F), while PV R2 was the top of a chimney-like structure devoid of microbial mat covering (G, H). Scale bars for images A, D, and F are 50 cm; scale bars for B, C, E, G, and H are 10 cm.

Fig. S5: Views of the Point Dume chimney field. A-E) the arrangements of several structures along the shallow sloping base of the Dume submarine canyon; all scale bars are approximately 1 m across at each photo's mid-point plane. F-I) Individual chimney structures 0.25-1m in height; scale bars are approximately 10 cm across at each photo's mid-point plane.

Fig. S6: Methane oxidation rates exhibited by sediment (PD PC2 0-5) and rock (PD R3) samples at varying methane concentrations. All samples were incubated at 7.58 MPa and measured using the CH_3D approach.

Fig. S7: Scanning electron microscope images of sample PD R1. A) Many putative framboidal pyrites (marked by white arrows) populate the rock interior. B) An aggregation of apparent cells (right) is in direct contact with a framboidal pyrite (left). The likely cell assemblage is very similar in size and shape to electron microscopy images of ANME-SRB consortia reported in studies such as McGlynn et al., 2018. C) and D) show aragonite fans within the rock.

Fig. S8: Control FISH images of intact interior portions of sample PD R1. Left: potential non-specific binding was tested by adding the non-Bact338-Cy3 probe. Right: potential autofluorescence was tested by not adding any fluorescent probes. Top panels show the rock surfaces; bottom panel overlays fluorescence channels used to visualize the Arch 915 and DSS 658 FISH probes, as in Fig. 3. All FISH protocol steps were followed.

Fig. S9: Histogram of number of mismatches between sequences derived from DADA2, Deblur, and UCLUST protocols and their nearest corresponding NCBI BLAST hit. Deblur was selected to generate the exact sequence variants reported in this study because it output the highest proportion of exact matches.

Fig. S10: Alpha diversity analyses of the 16S rRNA gene exact sequence variants derived from each sample's microbial community. Columns correspond to distinct samples grouped by geological setting; rows correspond to distinct alpha diversity metrics (see Supporting Information for additional details). Marker colors correspond to AOM rates; heat map key is shown at right.

Fig. S11: Beta diversity non-metric multi-dimensional scaling analyses using the 16S rRNA gene exact sequence variants and their relative abundances for all sequenced samples. Samples whose markers plot close to each other host relatively similar communities; more distant symbols indicate less similar communities. Each plot shows a distinct beta diversity metric (see Supporting Information for additional details). Symbol size corresponds to AOM rate, and symbol color indicates sample location.

Figure S1

Gulf of Mexico Sites

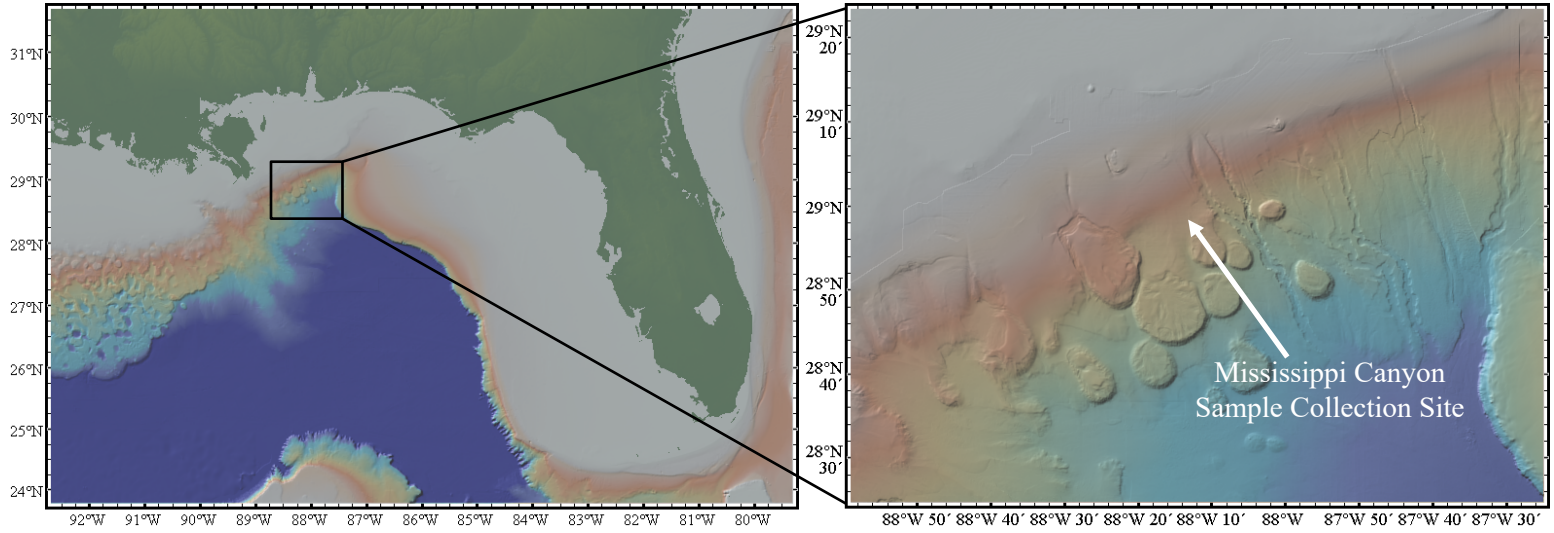

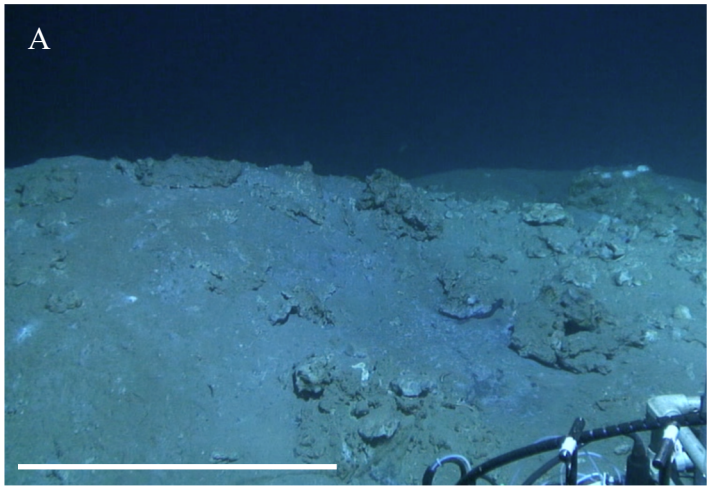

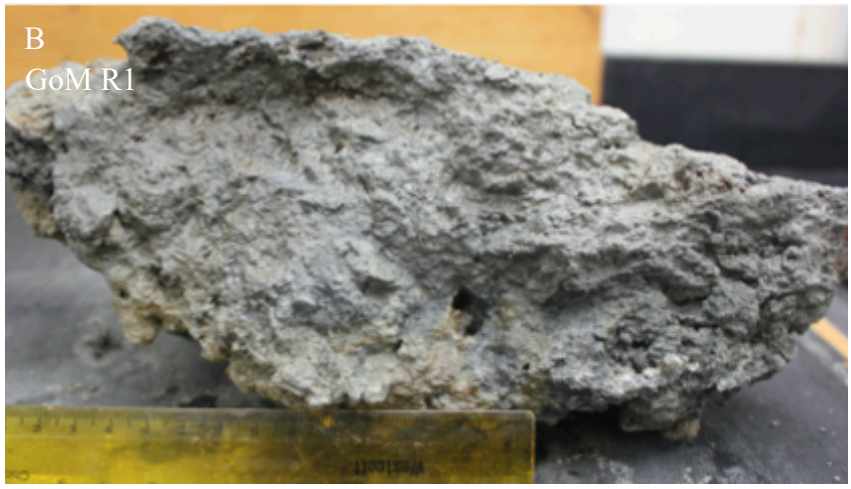

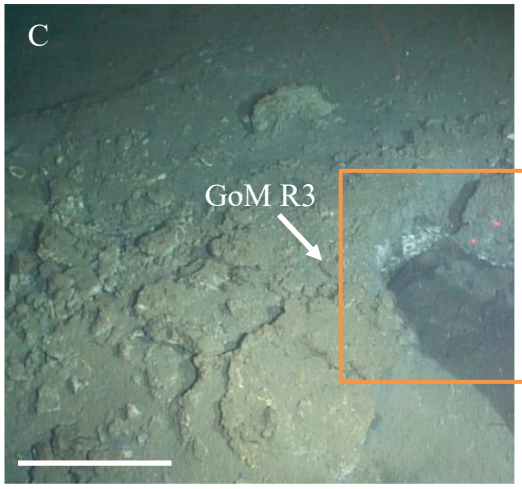

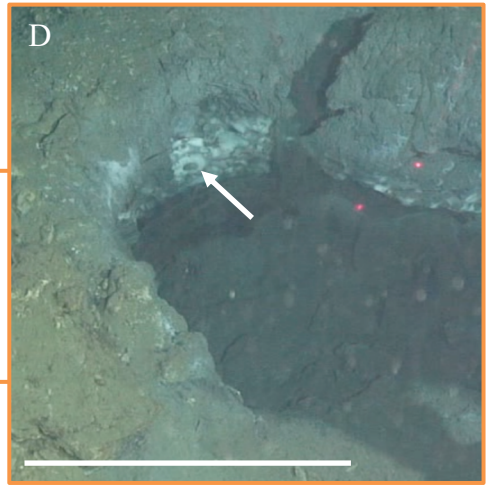

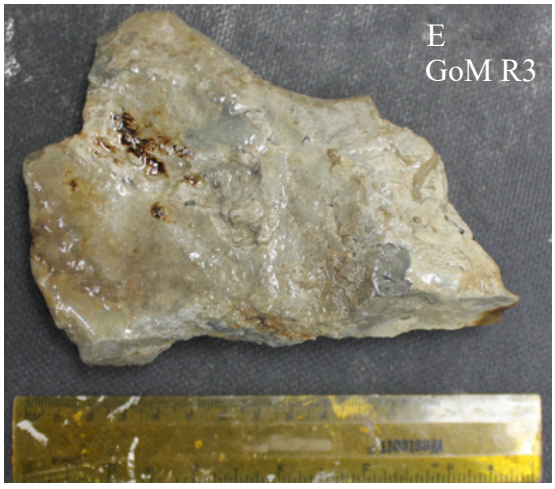

Figure S2

U.S. Atlantic Margin Sites

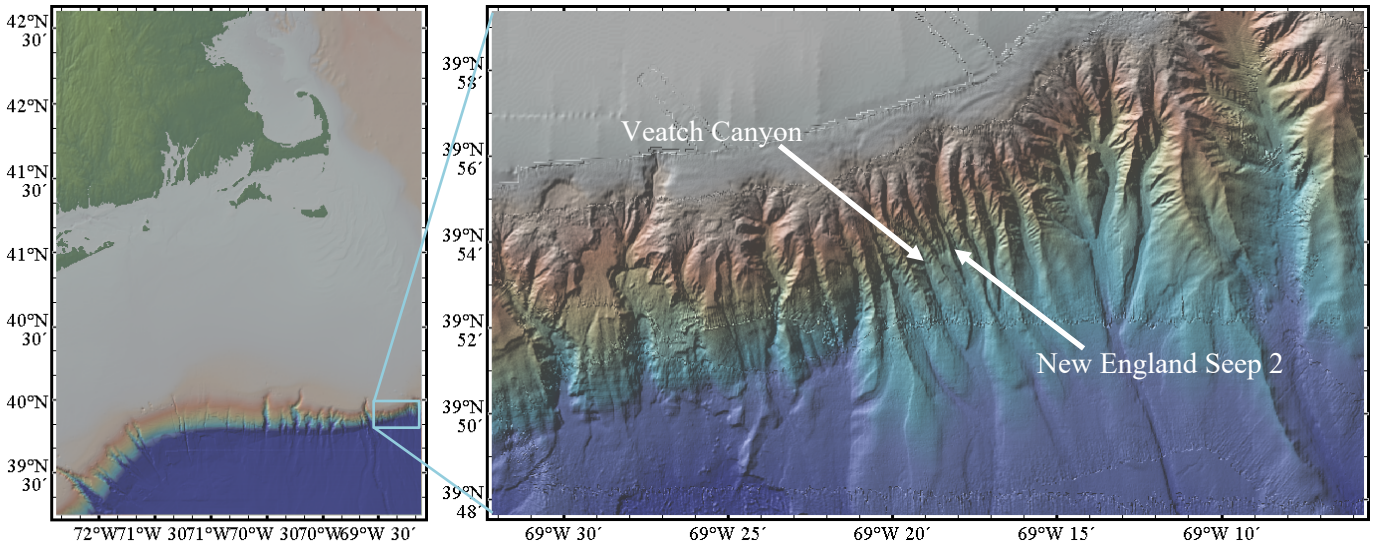

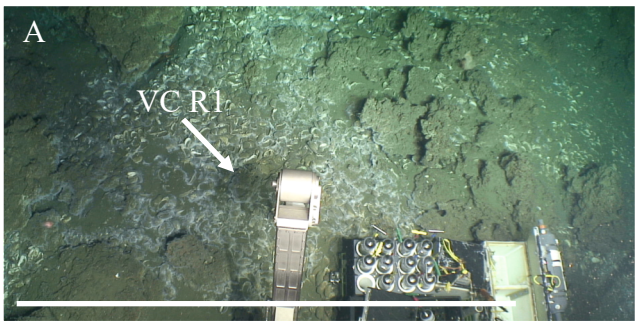

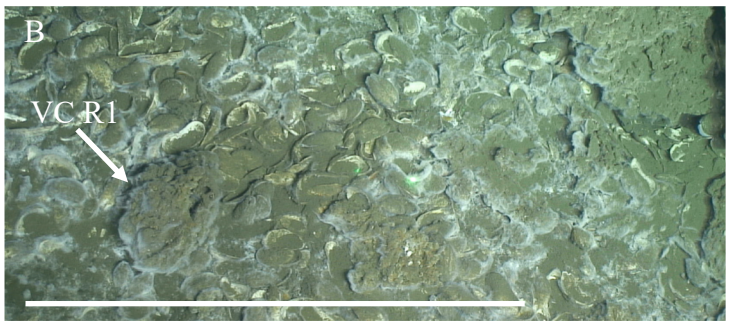

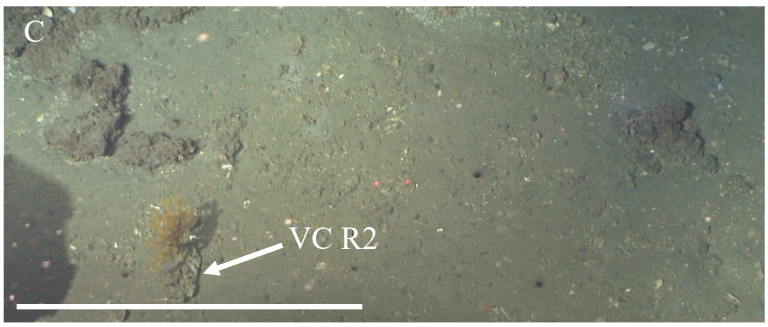

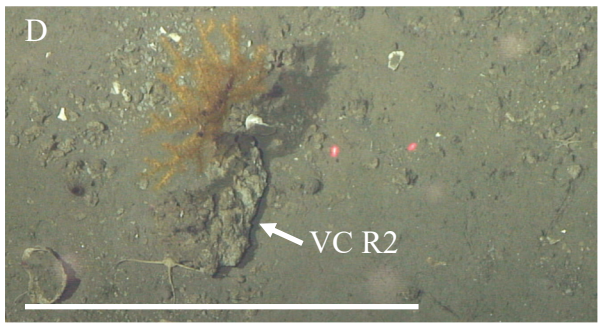

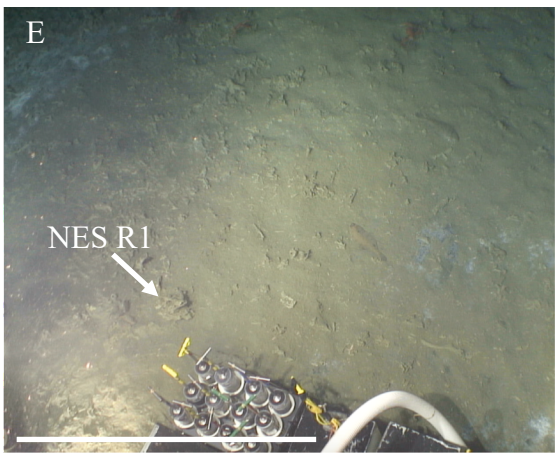

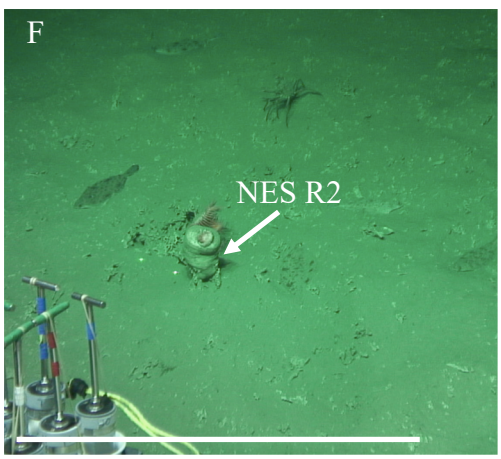

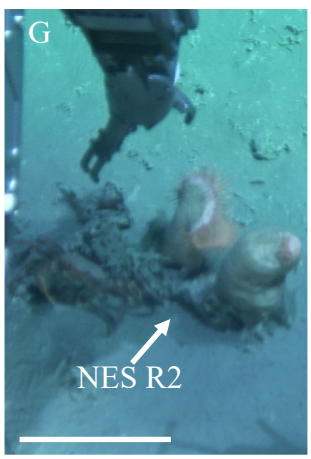

Figure S3

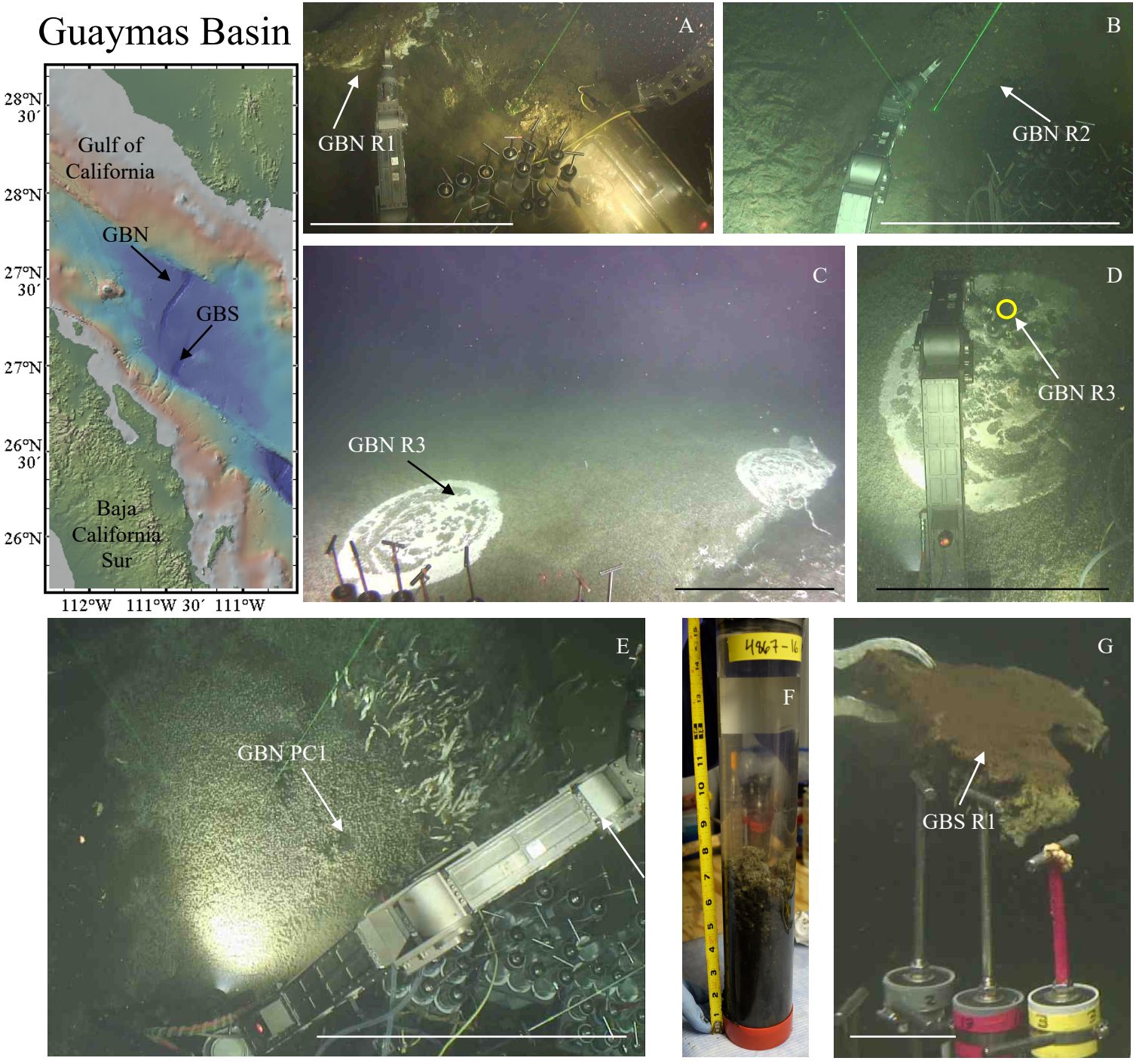
Guaymas Basin
28°N 30′
28°N
27°N 30′
27°N
26°N 30′
26°N
Gulf of California
GBN
GBS
Baja California Sur
112°W
111°W 30′
111°W
A
GBN R1
B
GBN R2
C
GBN R3
D
GBN R3
E
GBN PC1
F
4967-16
G
GBS R1

Figure S4

California Coast Sites

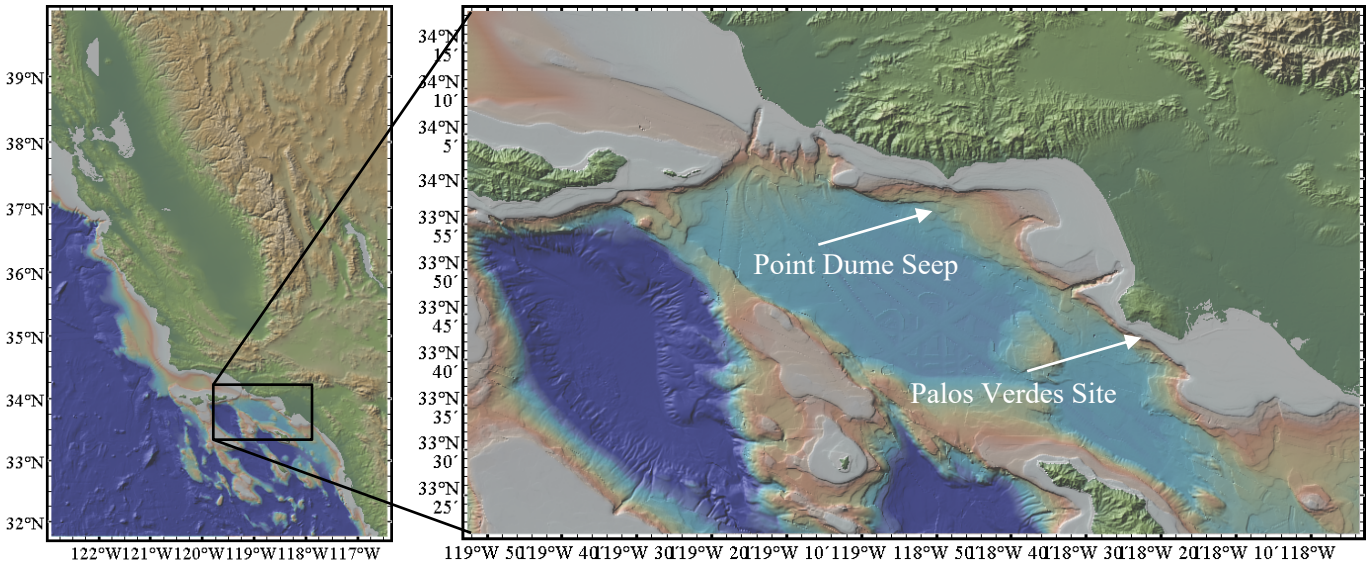

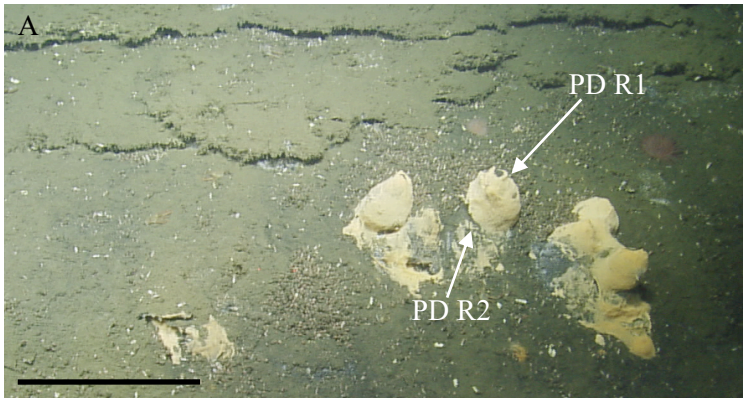

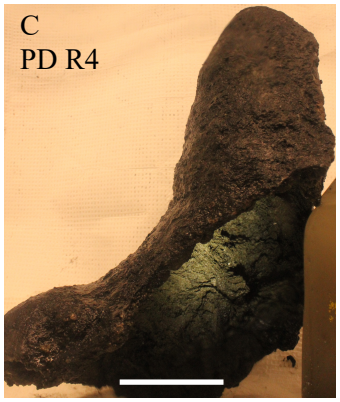

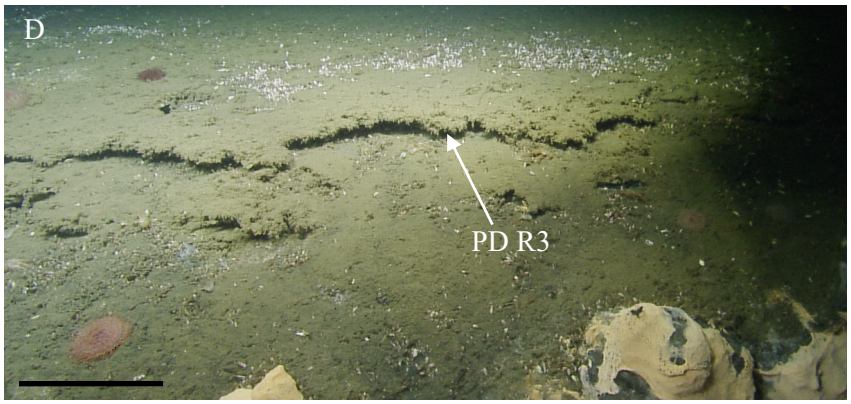

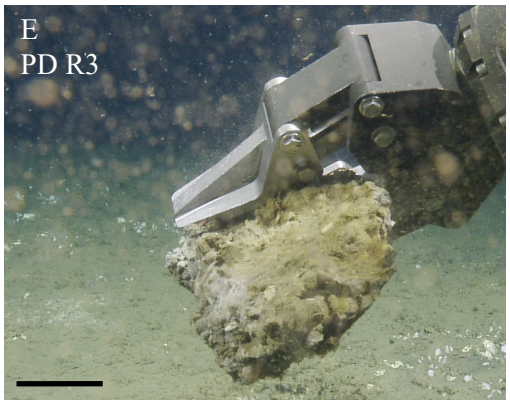

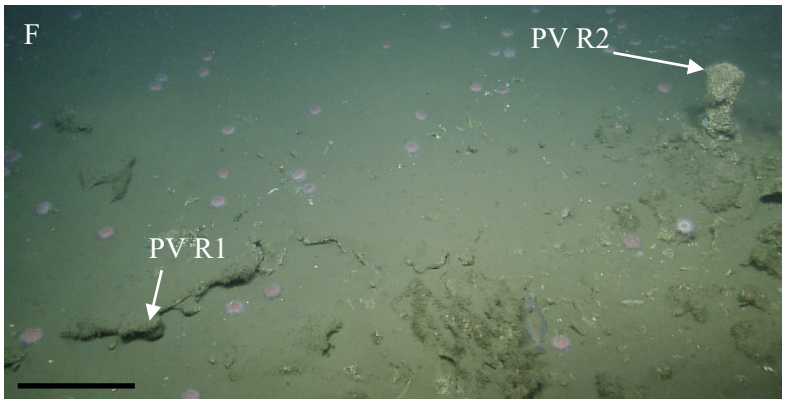

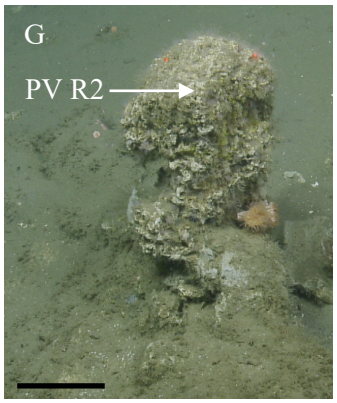

Figure S5

Point Dume Seep

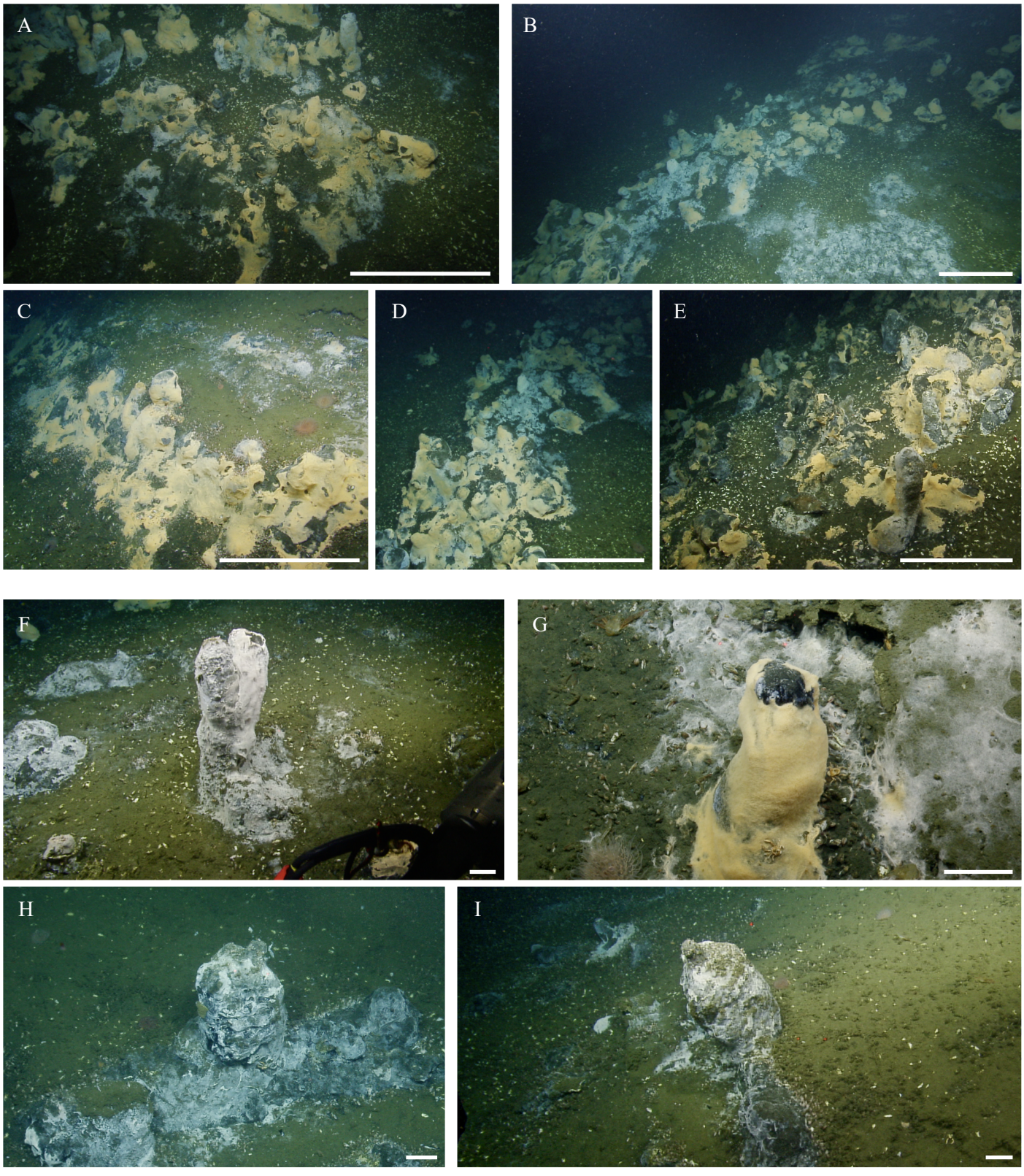

Figure S6

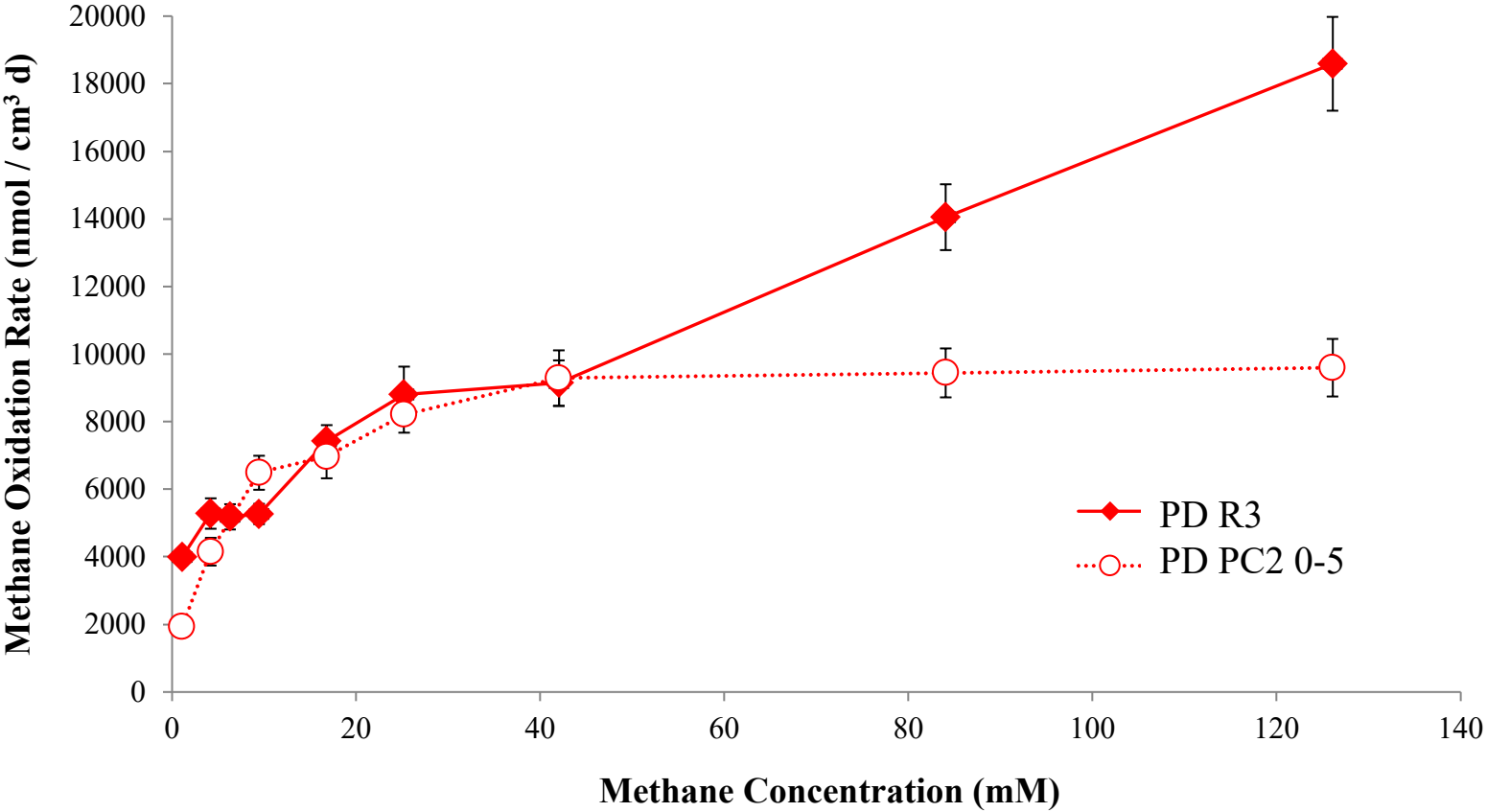
Methane Oxidation Rate (nmol / cm³ d)
20000
18000
16000
14000
12000
10000
8000
6000
4000
2000
0
0
20
40
60
80
100
120
140
Methane Concentration (mM)
PD R3
PD PC2 0-5

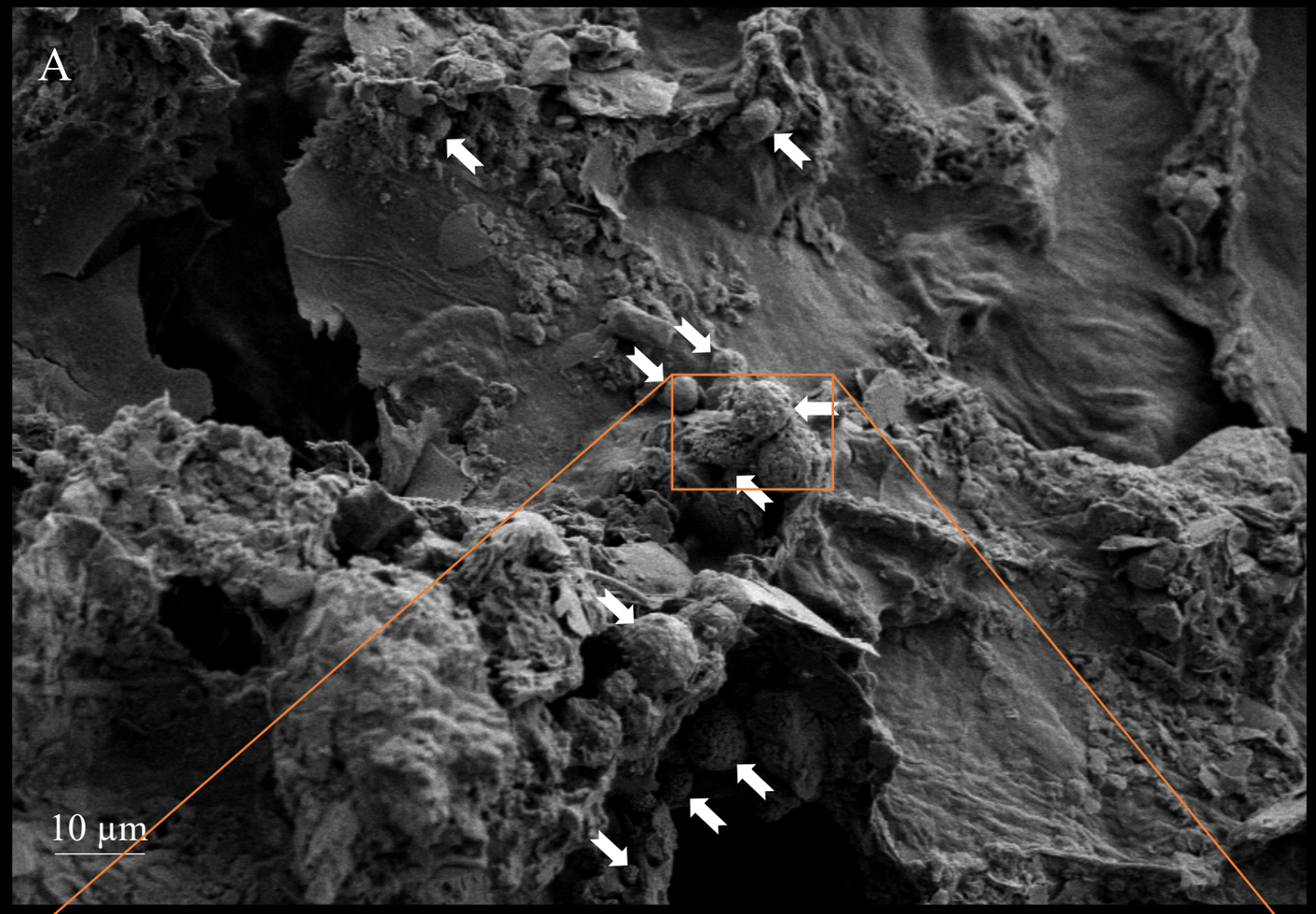
A
10 µm

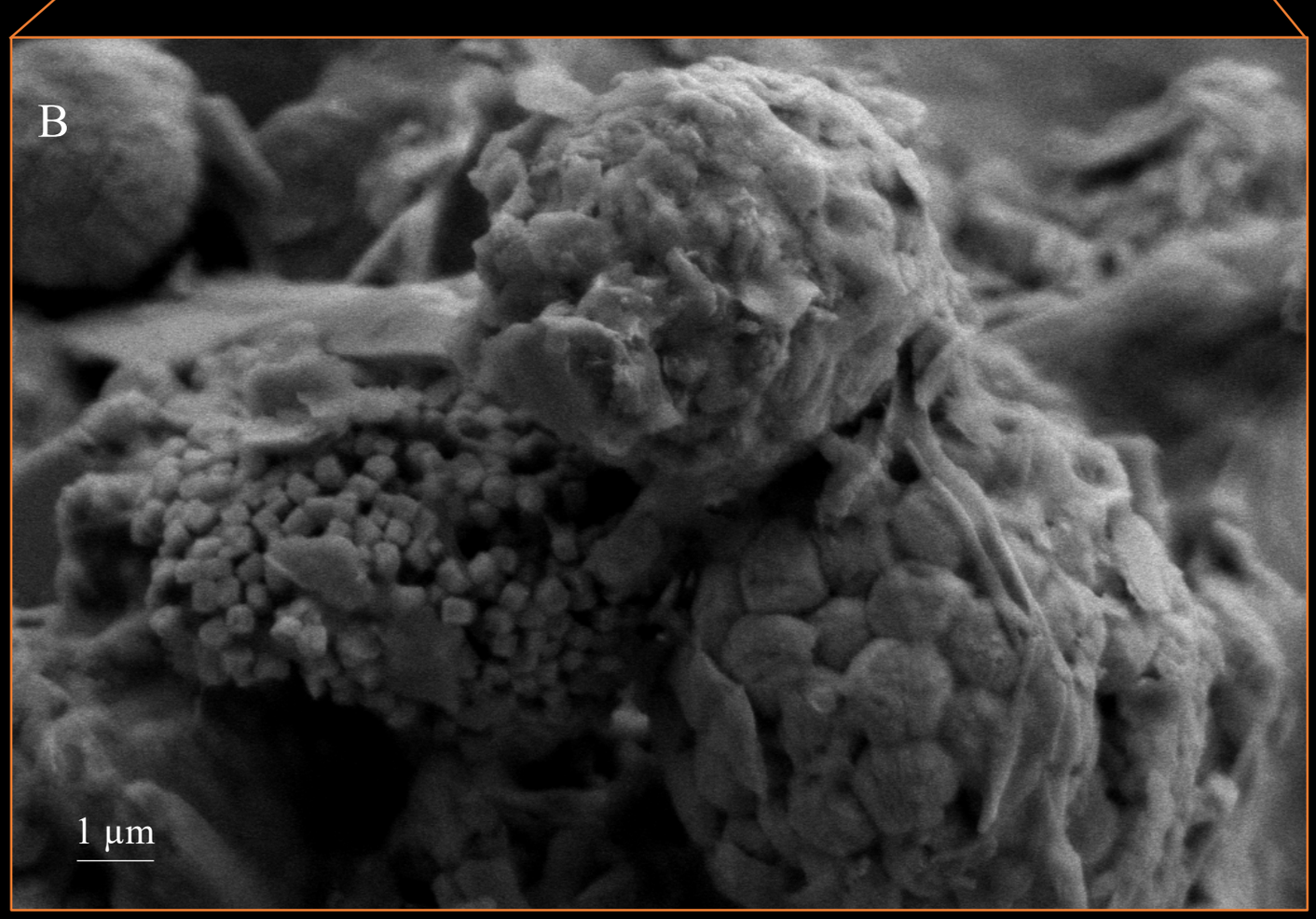
B
1 µm

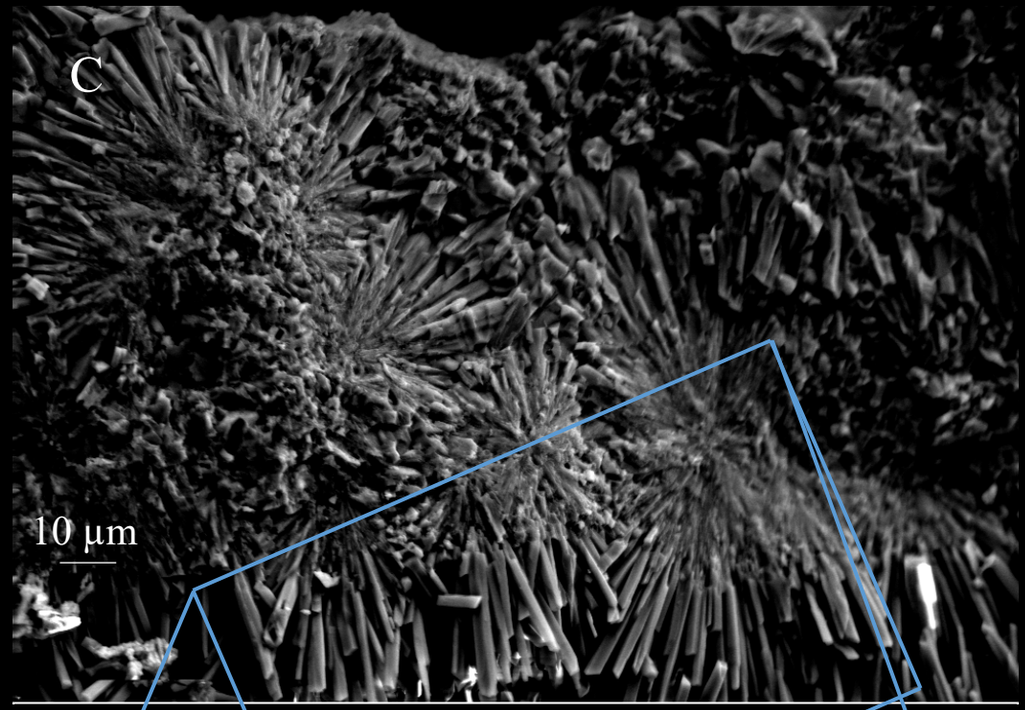
C
10 µm

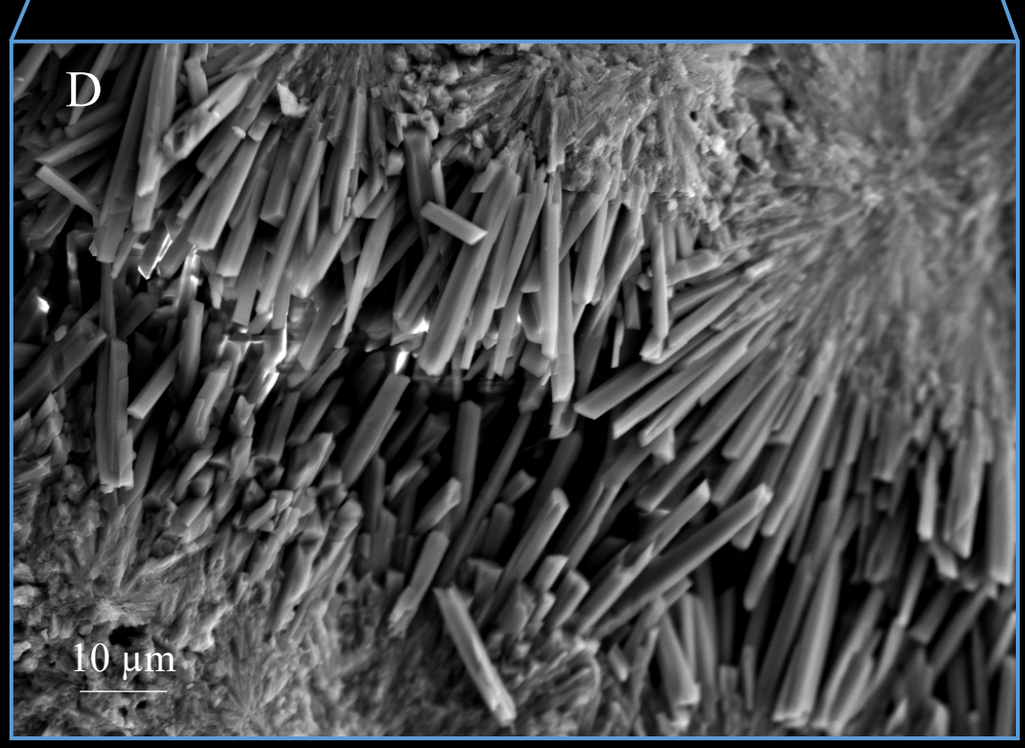
D
10 µm

Figure S8

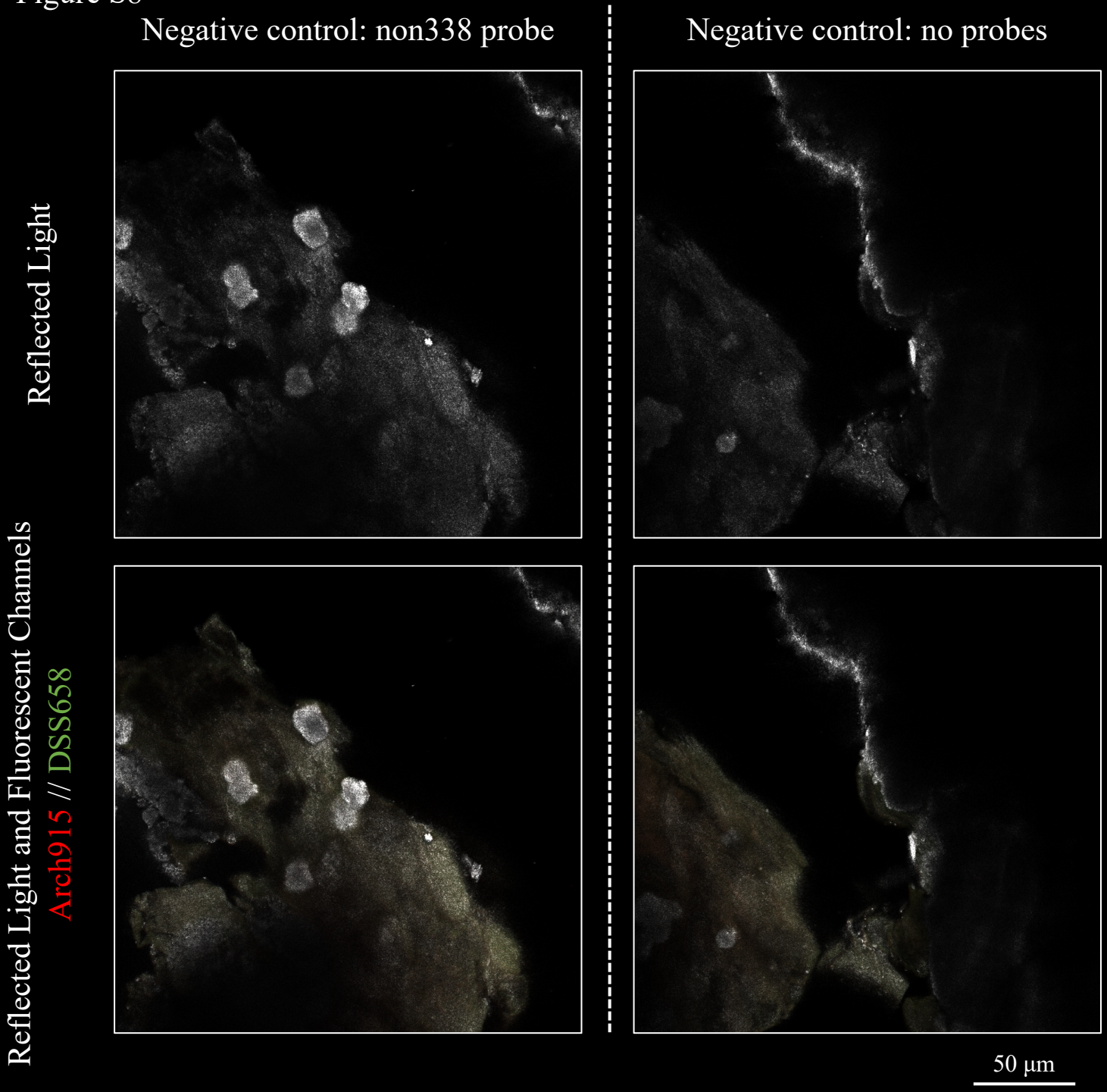
Negative control: non338 probe
Negative control: no probes
Reflected Light
Reflected Light and Fluorescent Channels
Arch915 // DSS658
50 µm

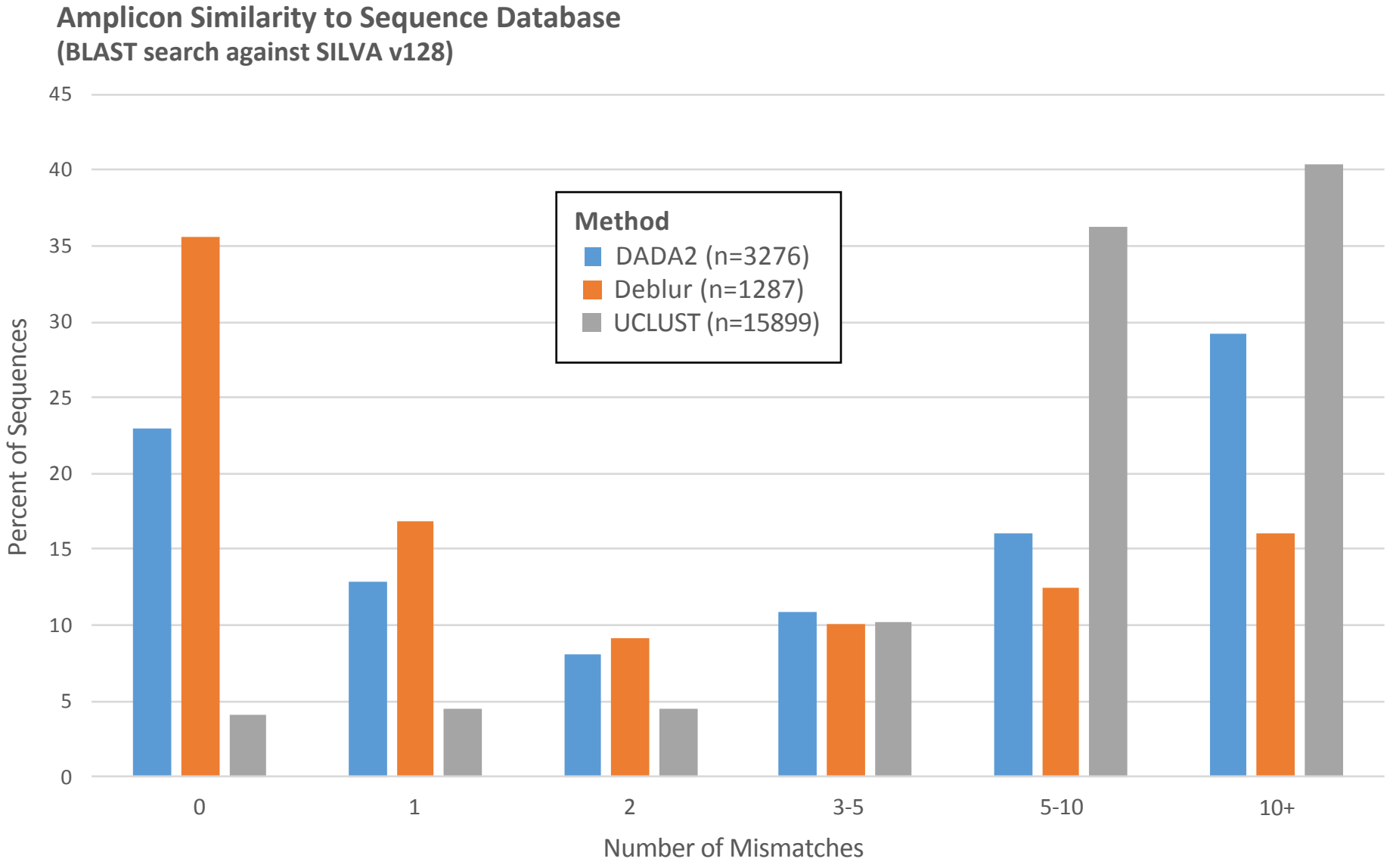
Amplicon Similarity to Sequence Database
(BLAST search against SILVA v128)
Percent of Sequences
45
40
35
30
25
20
15
10
5
0
Method
DADA2 (n=3276)
Deblur (n=1287)
UCLUST (n=15899)
0
1
2
3-5
5-10
10+
Number of Mismatches

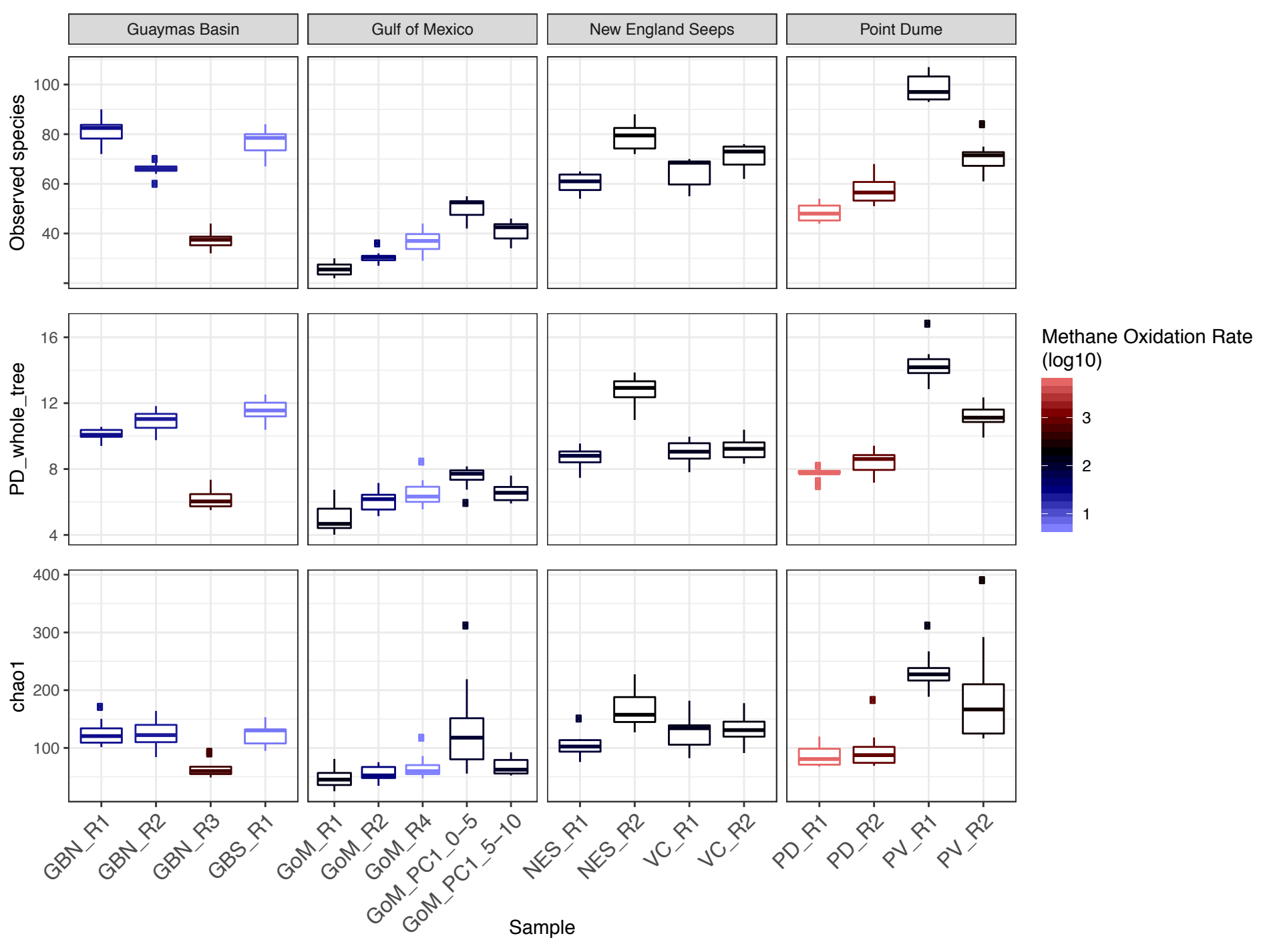
Guaymas Basin
Gulf of Mexico
New England Seeps
Point Dume
Observed species
PD_whole_tree
chao1
Methane Oxidation Rate (log10)
GBN_R1
GBN_R2
GBN_R3
GBS_R1
GoM_R1
GoM_R2
GoM_R4
GoM_PC1_0–5
GoM_PC1_5–10
NES_R1
NES_R2
VC_R1
VC_R2
PD_R1
PD_R2
PV_R1
PV_R2
Sample

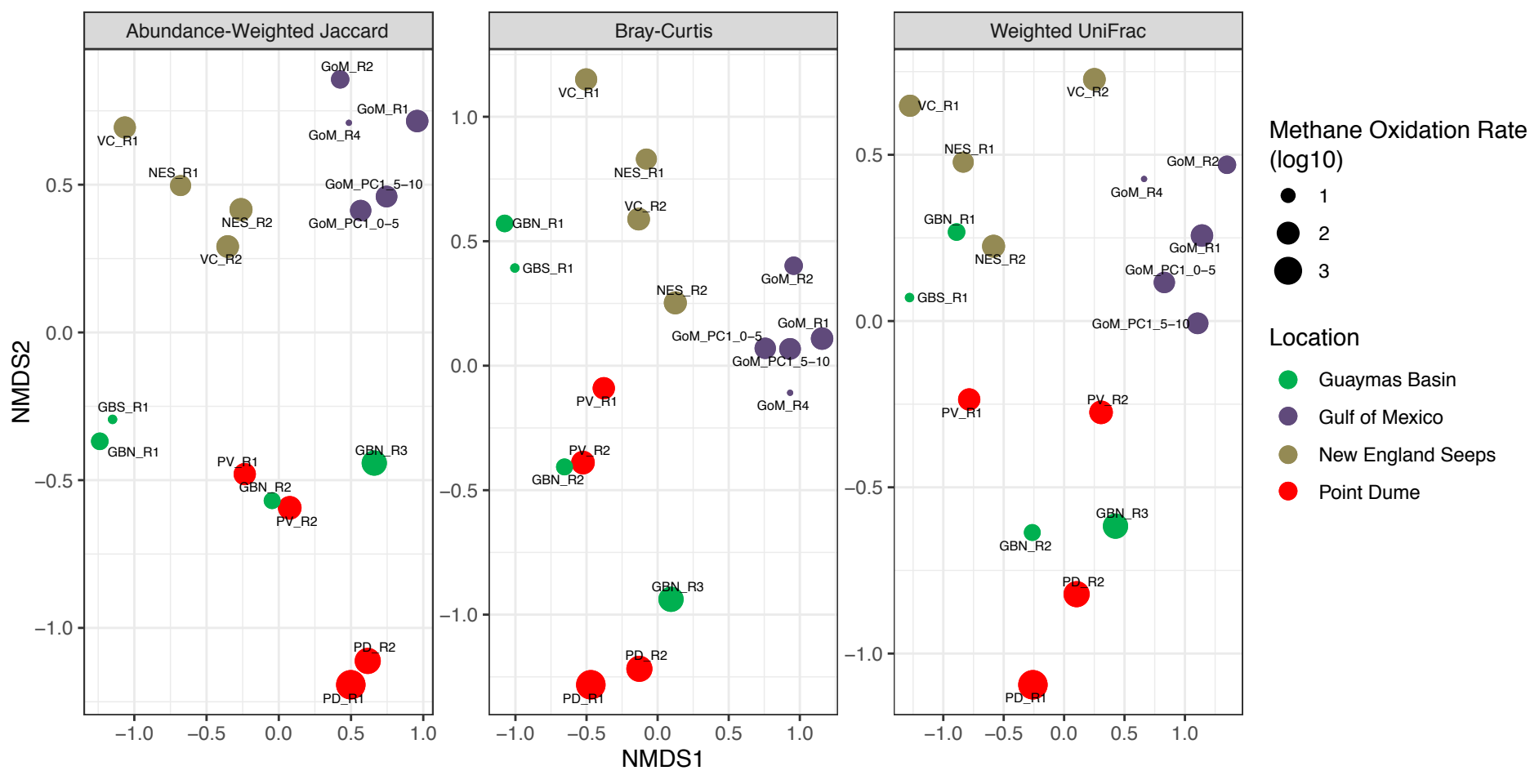
Abundance-Weighted Jaccard
Bray-Curtis
Weighted UniFrac
NMDS1
NMDS2
GoM_R2
GoM_R1
GoM_R4
VC_R1
NES_R1
GoM_PC1_5−10
NES_R2
GoM_PC1_0−5
VC_R2
GBS_R1
GBN_R1
GBN_R3
PV_R1
GBN_R2
PV_R2
PD_R2
PD_R1
Methane Oxidation Rate (log10)
1
2
3
Location
Guaymas Basin
Gulf of Mexico
New England Seeps
Point Dume

Table S1: AOM rate data from the side-by-side incubations using radiolabeled $^{14}CH_4$ and the CH_3D method. The sample-specific conversion factors, shown with their associated standard errors, were then applied to other samples' CH_3D-derived results to produce an "apparent", ^{14}C-equivalent, rate of AOM.

Sample Name	Incubation Time (d)	AOM Rate with $^{14}CH_4$	AOM Rate with CH_3D	D/H : ^{14}C ratio	Mean D/H : ^{14}C ratio conversion factor (SE)	Samples to which Conversion Factor was Applied
GoM R3a	3.125	879.86	1462.5	1.66	1.64 (0.06)	GoM R1, GoM R2, GoM R4
GoM R3b	3.125	1121.48	1723.3	1.54		
GoM R3c	3.125	1143.48	1976.8	1.73		
GoM PC2 5-10a	0.73	773.55	1702.7	2.2	2.14 (0.05)	GoM PC1 0-5, GoM PC1 5-10
GoM PC2 5-10b	0.73	641.68	1396.8	2.18		
GoM PC2 5-10c	0.73	1097.75	2239.3	2.04		
VC R1a	3.375	175.02	357.7	2.04	2.03 (0.05)	VC R2
VC R1b	3.375	173.42	367	2.12		
VC R1c	3.375	121.08	234.5	1.94		
NES R1a	3.375	115.46	229.81	1.99	1.96 (0.04)	NES R2
NES R1b	3.375	87.18	167.5	1.92		
GBN R1a	3.375	24.16	50.1	2.07	1.99 (0.09)	GBN R2, GBN R3, GBN PC1, GBS R1
GBN R1b	3.375	-3.98	20	NA		
GBN R1c	3.375	73.51	139.4	1.9		
PD R4a	0.73	3056.81	5864.2	1.92	1.82 (0.06)	PV R1, PV R2, PD R1, PD R2, PD R3
PD R4b	0.73	3610.67	6217.9	1.72		
PD R4c	0.73	3572.69	6533.3	1.83		
PD PC2 0-5a	3.125	451.06	855.3	1.9	1.97 (0.04)	PD PC1 0-5
PD PC2 0-5b	3.125	518.05	1020.7	1.97		
PD PC2 0-5c	3.125	595.56	1222.7	2.05		

Table S2: Mean methane oxidation rates and mineral phases of the samples analyzed in this study.

Geological Setting	Sample ID	Mean Short-term Methane Oxidation Rate (nmol / cm^3 d)	Mineral Phases from XRD		
			Major (> 25%)	Moderate (5-25%)	Minor (< 5%)
Sedimentary Basin	GoM R1	150.22	Mg calcite, quartz	chlorite, pyrite	dolomite
	GoM R2	34.09	Mg calcite	aragonite, quartz, greigite, illite, hydrotalcite	
	GoM R4	5	Mg calcite, illite	quartz	
	GoM PC1 0-5	98.21	Mg calcite, illite	quartz	
	GoM PC1 5-10	111.1	Mg calcite, illite	plagioclase, quartz	hydrotalcite
Passive Margin	VC R1	132.25	aragonite	quartz, illite, kaolinite	
	VC R2	166.54	aragonite	illite, quartz	orthoclase, kaolinite, albite, gypsum
	NES R1	85.62	aragonite	quartz, kaolinite, illite	calcite
	NES R2	193.23	aragonite	quartz, illite	kaolinite, orthoclase, albite
Hydrothermal Rift Basin	GBN R1	26.39	amorphous silica		
	GBN R2	21.67	aragonite		pyrrhotite, goethite
	GBN R3	537.75	aragonite	orthoclase	quartz, marcasite
	GBN PC1	22.06	illite, albite	quartz, amorphous silica	
	GBS R1	5.69	amorphous silica	barite	
Active Transpressional Margin	PV R1	140.72	feldspar	illite, quartz, calcite, pyrite, chlorite	
	PV R2	247.54	aragonite	illite, amphibole	quartz, phillipsite, greigite, chlorite
	PD R1 (exterior)	5528.27	aragonite	quartz, monohydrocalcite, amphibole, illite, chlorite	barite
	PD R1 (interior)		pyrite (> 80%)	illite, quartz	calcite
	PD R2	838.56	quartz, illite	magnesian calcite, albite	aragonite, feldspar, pyrite, hydrotalcite, montmorillonite
	PD R3	1561.66	Mg calcite, quartz	aragonite	pyrite
	PD R4	2884.39	Mg calcite, albite	pyrite, quartz	
	PD PC2 0-5	440.73	quartz	illite, albite, amphibole	calcite

Table S3: Conductance values for six seep samples. Conductance was calculated as the slope of a linear regression line through the -100 mV to 100 mV I-V data points for each sample.

Bulk Sediment Sample	**Conductance (Ω^{-1})**	**Mean Methane Oxidation Rate (nmol / cm^3 d)**
GoM PC1 0-5	3.00×10^{-9}	98.2
PD R2	1.73×10^{-9}	838.6
PD R3	1.71×10^{-9}	1561.7
PD PC2 0-5	1.54×10^{-9}	440.7
GBN R1	1.24×10^{-9}	26.4
GoM R1	7.32×10^{-10}	150.2

Table S4: Methane oxidation rates of incubations using a range of particle sizes of the PD R3 carbonate rock. Experiments were performed in triplicate, and kept at 4 ºC for 8 days. Values were measured using the CH_3D approach and corrected to apparent rates using the site specific ^{14}C rate conversion factor from Table S2. Note: "a/c" refers to the autoclaved negative control sample.

Sample	**Mean Fragment Size (µm)**	**Mean Apparent AOM Rate (Standard Deviation; all values in nmol / cm^3 d)**
PD R3 (A)	20,000 - 25,000	1099.89 (179.95, n=3)
PD R3 (B)	5,000 - 7,000	1051.1 (435.8, n=3)
PD R3 (C)	~2,000	1180.11 (123.22, n=3)
PD R3 (D)	~400	1089.89 (251.26, n=3)
PD R3 (a/c)	20,000 - 25,000	-47.69 (12.3, n=3)

Table S5: Cell abundance values derived from DAPI counts of selected sediment and rock samples before and after the long-term incubation experiments.

Sample	Mean Methane Oxidation Rate (nmol / cm^3 d)	Cell Abundance (# / cm^3 substrate)		Change in Cell Abundance (#/cm^3 substrate)
		Pre-Incubation	Post-Incubation	
PD R4	2884.39	6.20E+08	1.24E+09	6.20E+08
PD R1	5528.27	3.89E+08	8.77E+08	4.88E+08
GoM R3	885.81	4.88E+08	7.35E+08	2.47E+08
PD R3	1561.66	2.21E+08	5.91E+08	3.70E+08
PD PC2 0-5	440.73	1.27E+08	4.86E+08	3.59E+08
VC R1	132.25	3.07E+08	2.85E+08	-2.20E+07
GBN R3	537.75	NA	2.10E+08	NA
GBN PC1	22.06	2.08E+08	1.63E+08	-4.55E+07
PV R1	140.72	1.51E+08	1.48E+08	-3.00E+06
NES R1	85.62	1.89E+08	1.13E+08	-7.60E+07
GBN R1	26.39	1.13E+08	8.09E+07	-3.21E+07
GoM R1	150.22	NA	8.01E+07	NA

Table S6: Results of PERMANOVA statistical test of samples by location, lithology, mineralogy, and categorized methane oxidation rates. *Note: Values used to categorize methane oxidation rate measurements: high: 1000+, med-high: 500-1000, med: 50-499, low: <50.

Distance metric	Location	Mineralogy	Lithology	Methane Oxidation Rate*
Jaccard (binary)	0.001	0.01	0.027	0.004
Bray Curtis	0.001	0.036	0.04	0.018
UniFrac (unweighted)	0.001	0.008	0.103	0.01

Table S7: Results of Mantel correlation tests with methane oxidation rate as the categorical variable.

Distance metric	r statistic	p-value
Jaccard (binary)	0.192	0.01
Bray Curtis	0.169	0.067
UniFrac (unweighted)	0.281	0.002

Table S8: Headspace composition introduced to reach the designated dissolved methane concentration at 7.58 MPa. *Note: methane consisted of 50% CH_4 and 50% CH_3D by volume.

Dissolved methane concentration at 7.58 MPa	**Proportion of methane* in headspace (balance nitrogen)**	**Overall quantity of methane (nmol)**
129 mM	100.0%	4.5E+06
86.0 mM	66.7%	3.0E+06
43.0 mM	33.3%	1.5E+06
25.8 mM	20.0%	8.9E+05
17.2 mM	13.3%	5.9E+05
9.7 mM	7.5%	3.3E+05
6.5 mM	5.0%	2.2E+05
4.3 mM	3.3%	1.5E+05
1.1 mM	0.9%	4.0E+04

Table S9: Sechenov equation parameters for methane and the ions found in seawater. c_i values are derived from ion abundances reported in Millero et al., 2008, and seawater density at 4 °C was calculated per Millero & Poisson, 1981. h_i and h_g values are from Weisenberger & Schumpe, 1996. Ions for which no hi was available were not included in the calculation.

Ion	c_i (mol / L)	h_i (m^3 / kmol)
Na^+	4.82E-01	0.1143
Mg^{2+}	5.43E-02	0.1694
Ca^{2+}	1.06E-02	0.1762
K^+	1.05E-02	0.0922
Sr^{2+}	9.31E-05	0.1881
Cl^-	5.61E-01	0.0318
SO_4^{2-}	2.90E-02	0.1117
HCO_3^-	1.76E-03	0.0967
Br^-	8.65E-04	0.0269
CO_3^{2-}	2.45E-04	0.1423
$B(OH)_4^-$	1.03E-04	NA
F^-	7.02E-05	0.092
OH^-	8.19E-06	NA
Gas Species	h_g (m^3 / kmol)	
CH_4	0.0022	